UNIVERSITY OF OKLAHOMA

GRADUATE COLLEGE

ASSESSING THE IMPACT OF NON-CONVENTIONAL OBSERVATION TYPES

ON HIGH-RESOLUTION 3DVAR ANALYSES AND ARW-WRF FORECASTS

A THESIS

SUBMITTED TO THE GRADUATE FACULTY

in partial fulfillment of the requirements for the

Degree of

MASTER OF SCIENCE IN METEOROLOGY

By

ANDREW OSBORNE
Norman, Oklahoma
2016

ASSESSING THE IMPACT OF NON-CONVENTIONAL OBSERVATION TYPES
ON HIGH-RESOLUTION 3DVAR ANALYSES AND ARW-WRF FORECASTS

A THESIS APPROVED FOR THE
SCHOOL OF METEOROLOGY

BY

_____
Dr. Frederick Carr, Chair

_____
Dr. Keith Brewster

_____
Dr. Xuguang Wang

Acknowledgements

I would like to thank my advisors Dr. Frederick Carr and Dr. Keith Brewster, for their guidance and help through the research process. Their expertise in the areas of data assimilation and data impact studies was a vital resource for me in conducting and analyzing the experiments presented here.

I also want to recognize Dr. Derek Stratman for providing guidance on verification methods used here. Dr. Xuguang Wang also played an important role in reviewing the thesis and providing feedback as a member of the thesis committee.

Fellow graduate student Lee Carlaw was very helpful here as he provided a lot of guidance on the computer programming aspect of setting up these experiments.

Table of Contents

List of Tables

List of Figures

Abstract

This work looks at the impact on high-resolution analyses and forecasts of several non-conventional data types available within the Dallas Fort Worth (DFW) Urban Testbed. A major focus is an evaluation of the added value of the Center for Collaborative Adaptive Sensing of the Atmosphere (CASA) X-band radar network in the DFW area. The impact of this radar data is compared to that of the other radar networks in the area including the Next-Generation (WSR-88D NEXRAD) radars and the Terminal Doppler Weather Radars (TDWRs). Data denial experiments are performed using the Advanced Regional Prediction System (ARPS) Three-Dimensional Variational (3DVAR) analysis system and the Advanced Research Version of the Weather Research and Forecasting Model (ARW-WRF). Cycled data assimilation is performed on a 1 km grid with subsequent forecast performed on a 400 m grid. The case chosen is the 26 December 2015 tornado outbreak in north-central Texas with specific focus on model simulations of the Rowlett tornadic supercell. Verification results and comparison among data denial experiments show that the WSR-88D radar network appears to supply the most important data for this case. Forecasts of reflectivity (verified via fractions skill score (FSS)) and low-level rotation (0-1 km updraft helicity tracks verified via object-based track error algorithm) were able to accurately capture the storm evolution but only when the WSR-88D radar data was included. The Rowlett storm is on the edge of the shorter-range CASA and TDWR networks and so these radars are not able to provide sufficient observations to initialize the storm properly in the model. A noticeable increase in rotational intensity in the forecasted storm, possibly to unrealistic values, is found when CASA radar data is

denied from the control experiment. Comparison of model quantitative precipitation forecast (QPF) output with observed rainfall estimates indicate a wet bias in the model used here which makes the precipitation forecasts less useful than the rotational forecasts. A separate experiment focus on surface observation impact found substantial positive impact of non-conventional surface observations on frontal placement southwest of the DFW metropolitan area.

Chapter 1

1.1 Motivation

In 2003, a workshop convened to discuss the current state of the national meteorological observing network. The observation network serves many different purposes, one of which is to create the initial conditions for numerical weather prediction (NWP) forecasts. The characteristics of the observation network, such as the density and quality of observations, are directly related to the quality of forecasts initialized from those observations (Dabberdt et al. 2005). The conclusions from the workshop included a need for improvements to the existing mesoscale observing network to better leverage the improved capabilities of numerical models to make high-resolution analyses and forecasts of high impact weather events (Dabberdt et al. 2005). The lowest levels of the atmosphere are seen as the highest priority for the improvements to the network, as there is a dearth of observations in this important region closest to the surface. Better characterization of the structure of important phenomena (fronts, boundary layer processes, outflow boundaries, dry lines, etc.) in this currently poorly sensed layer will lead to better analyses and forecasts of high-impact mesoscale events. Dabberdt et al. (2005) proposed more frequent and dense observations from surface stations (a minimum station spacing distance of 25 km over a nationwide network with 10 km spacing in particularly challenging areas such as heavily populated cities, coastal regions, or mountainous terrain). Also low power X-band (3 cm wavelength) radars stationed in gaps between the current S-band (10 cm wavelength) Next-Generation Radar (WSR-88D NEXRAD) network have been

proposed to enhance observation of the lowest levels of the atmosphere. The Center for Collaborative Adaptive Sensing of the Atmosphere (CASA) has developed such radars to demonstrate the effectiveness of these high-resolution observations within testbeds in southwest Oklahoma and the Dallas Fort Worth (DFW) metropolitan area (McLaughlin et al. 2009).

It has been recognized that in order to realize the full benefits of higher spatial and temporal resolution of the atmosphere, it is necessary to not only establish new observing systems but to also unify the existing amalgamation of networks throughout the nation. A National Research Council (NRC) report entitled *Observing Weather and Climate from the Ground Up: A Nationwide Network of Networks*, proposed a nationwide Network of Networks (NoN) which would link together the chaotic, fragmented assortment of mesoscale observations from private, public, and academic providers into one coherent, coordinated national observing system (National Research Council 2009). They concluded that there are a multitude of non-federal observing networks which contain potentially valuable meteorological information for a variety of end users. These resources have not been leveraged effectively due to a lack of a centralized voice encouraging the utilization of all these observations in an efficient manner. Among private, public, and academic interests, the government is seen as the most appropriate to lead the unification process. The goal is to bring together organizations with networks that serve different interests into one unified observation network with specific metadata, communication, instrumentation, and siting standards. With this goal in mind, the NRC report proposed the use of research testbeds in different areas of the country to demonstrate the potential benefits of a more

coordinated approach before applying it on a national scale (National Research Council 2009).

1.2 DFW Urban Demonstration Network

One testbed put in place to serve this purpose is the DFW Urban Demonstration Network (National Research Council 2012). This testbed was brought about via a partnership between local municipalities, private companies, academic institutions, and the National Weather Service (NWS). To date, seven of eight planned X-band radars have been deployed around the DFW metropolitan area to augment the low-level radar coverage provided by the S-band KFWS WSR-88D radar. A smaller network of four X-band radars was deployed in southwest Oklahoma in 2007, a project known as CASA Integrated Project-1 (IP-1) and the extra data provided was useful for detection of atmospheric phenomena providing positive benefit to the NWP forecasts which incorporated them (Brewster et al. 2007; Schenkmann et al. 2011; Snook et al. 2012). The National Science Foundation (NSF) CASA Engineering Research Center (McLaughlin et al. 2009) developed the radar networks in both areas. In the DFW testbed, the eight planned X-band radars, the WSR-88D NEXRAD radar in Fort Worth, two Federal Aviation Administration (FAA) C-band Terminal Doppler Weather Radars (TDWRs), satellite data, aircraft data in air and during take-off/landing, radiosonde data, radiometer data, and several surface observing networks allow for tremendous data coverage. The DFW metro area was deemed to be a good candidate for this type of project due its large population (over 6.5 million people), several major interstates, two major passenger airports, and the resultant impacts on people and property caused by

the various types of hazardous weather that occur there. These hazards include hail, severe storm winds, flash flooding, ice storms and even the occasional tropical system. Successes and challenges within this endeavor will be useful in refining the approach for future testbeds and eventually in a national network. One aim of this testbed is to assess impacts of a more cohesive observing network on high resolution NWP forecasts. In this work, the impact of several observation types within the context of the entire network will be examined via several observing system experiments.

1.3 X-band radars

The dense network of low power 3 cm radars in the DFW testbed allows for better coverage in areas where the WSR-88D observing network lacks observations (below the lowest radar tilt and directly above the radar sites). Horizontal resolutions of 100 m combined with up to 5 times faster update speeds with adaptive scanning strategies (McLaughlin 2009) allow for improved awareness of dangerous weather. Also, this increased coverage allows for more detailed, faster updating analyses for operational and research-based forecasts. The CASA IP-1 deployment of four radars in southwest Oklahoma served as an example of the potential viability and forecast impact such observations could have. From those promising results, an expanded X-band radar network in DFW was planned to gauge the potential effects of the gap-filling radars in a highly-populated, urban area. This network includes X-band radars from multiple sources including CASA and private companies. Although the original vision was a national network of CASA radars spaced 30 km apart on cell-phone towers and buildings (McLaughlin 2009), this urban testbed serves as an initial example for

potential expansion of CASA radar networks to other major cities or weather sensitive areas that may have gaps in the NEXRAD radar network. .

1.4 Observing System Experiments

In the context of the proposed NoN vision, it is crucial to understand which observation types within an expanding network will be most impactful. This allows informed decisions to be made about the most important observations to invest in when deploying a potential national observing network. A commonly used approach to assess observation impact in NWP models is the observing system experiment (OSE). The classic OSE involves a control run which assimilates all available observational data to produce an analysis and forecast. A subsequent set of analyses and forecasts are run each of which deny assimilation of observations from a certain type and the results of this run are compared to the control run. The magnitude of difference in errors among the runs serves as a measure of the benefit afforded to the forecast by the observation type that was denied. OSEs can be expensive to run for all permutations of different observation types that need to be tested, and there is an emerging method called Forecast Sensitivity to Observations (FSO) (Cardinali 2009), which can calculate the impact of all observation types at the same time in one run. An observation type may show a lack of impact for a particular case, such as in McNally (2013) where geostationary satellite data did not seem to contribute substantially to the accurate forecast of the track of Hurricane Sandy. For that same case, the polar-orbiting satellite data showed a strong positive impact on the prediction of the track of the storm.

Most of the OSE work to this point has focused on the impact of observations available in the federal network such as satellite radiances and derived winds (Bouttier and Kelly 2001; Zapotocny et al. 2002,2005,2007; Kazumori et al. 2008; Bi et al. 2011), sounding/profiler data (Graham et al. 2000; Benjamin et al. 2010; Agusti-Panareda et al. 2010), aircraft measurements (Benjamin et al. 2010), and radar data (Schenkman et al. 2011a, 2011b). One of the few studies to address the impact of non-federal observation types is Tyndall and Horel (2013), which found the most important factor governing observation impact was the proximity to other observations. Assimilation of observations in data-sparse areas provided new information to constrain the model state, especially during periods where predictability was low, regardless of the observation type. From this result, the CASA radar data assimilated in this thesis, being in the relatively data-sparse lowest levels of the atmosphere, would be expected to provide some value to the analyses and forecasts, particularly in areas well displaced from the Fort Worth NEXRAD radar. Hilliker et al. (2010) found improvement to short-term operational National Digital Forecast Database (NDFD) forecasts of temperature and dew point from inclusion of Automated Weather Source (AWS) Weatherbug surface observations in the assimilation process. Forecasts of wind did not show any improvement with the added AWS observations. Carlaw (2014) found a similar impact from Citizen Weather Observer Program (CWOP) and AWS Weatherbug surface observations on high-resolution analyses and forecasts within the DFW demonstration network. The low impact from the additional wind observations is likely due to sub-standard siting for many of these stations (many are on rooftops or not in open areas). This work will focus on the observation impact of several non-conventional observation

types on the forecast of a case involving a supercell thunderstorm which produced an EF4 tornado near Rowlett, TX on 26 December 2015.

1.4.1 Radar OSEs

The network of X-band radars installed in the DFW area generally provides better coverage in the lower third of the troposphere compared to the much more widely spaced WSR-88D network, whose beams only "see" the lowest levels very close to the radar location. Radar assimilation has been shown to result in more accurate model representations of frontal boundaries, dry lines, gust fronts, boundary layer structure, and other important mesoscale features. Higher resolution radar data allows for better use of the increased resolution of today's NWP models, allowing more precision and accuracy in capturing the key features that control convective scale storm evolution. Assimilation of additional reflectivity and radial velocity data from four CASA radars was shown to result in more accurate analyses and forecasts during several studies performed within the context of the IP-1 CASA radar deployment in southwest Oklahoma. Schenkmann et al. (2011) found that assimilation of radial velocity data from the CASA radars in the area resulted in a more accurate analysis and subsequent forecast of the wind field for a mesoscale convective system (MCS) with a line end vortex. The finer scale structure of the wind field resolved by the CASA velocity data allowed for slowing of the cold pool, increased shear ahead of the gust front, and subsequent vertical vorticity increase near a boundary intersection in the vicinity of an observed tornado. The CASA velocity data was able to augment the kinematic information provided by the surface Oklahoma Mesonet stations to more fully resolve the detailed pattern of the gust front. It was also found that assimilation of CASA radar

data from the IP-1 deployment in a tornadic case resulted in a greater probability of ensemble forecasts having a low-level vortex in the vicinity of an observed tornado (Snook et al. 2012). The inclusion of radar data assimilation in Xiao and Sun (2007) resulted in better representation of a squall line and associated cold pool structures, resulting in more accurate intensity and propagation speed estimates by the model.

Xiao and Sun (2007) found that assimilation of reflectivity primarily improved the model representation of the hydrometeor variables, while the assimilation of radar radial velocity primarily improved the model wind field. A similar demarcation of impact was found for a tropical cyclone case (Zhao and Xue 2009), where radial velocity assimilation increased the track accuracy while reflectivity assimilation increased the accuracy of the strength estimate. The effect of radial velocity and reflectivity will also be assessed separately in the present work to determine if these assertions hold for the high-resolution forecasts of the 26 December tornadic event.

Several studies have looked at the impact of radar assimilation on model Quantitative Precipitation Forecast (QPF) estimates, as the radar data allows a better representation of mesoscale structures and more accurate forecasts of precipitation-producing storms. Xiao and Sun (2007) found radar assimilation enhanced QPF accuracy, as the squall line structure for their case was better represented in the model. Radar data assimilation was shown to have a positive impact on 1 km convective-allowing forecasts of precipitation over the entire continental United States in Xue et al. (2013). The forecasts were generated with the Advanced Research Version of the Weather Research and Forecasting model (ARW-WRF) along with Advanced Regional Prediction System (ARPS) Three Dimensional Variational (3DVAR) data assimilation

8

with complex cloud analysis, which is the same configuration used in this thesis. One objective of the CASA radar deployment and urban demonstration network is to improve flash flood forecasts in NWP and hydrologic models with the added data availability. To address this goal, this work will examine how the accuracy of model QPF estimates changes with assimilation of some or all of the CASA radars.

One notable benefit of radar assimilation is faster replication of pre-existing precipitation information in the model. Dawson and Xue (2006) found a decreased spin-up time of 2-3 hours with radar data assimilated in intermittent cycles for an MCS case using the ARPS forecast model and ARPS Data Analysis System (ADAS). Hu et al. (2006) found a decrease in timing and location errors for a tornadic thunderstorm in the Fort Worth area with inclusion of radar data incorporated via a complex cloud analysis in the assimilation process. The forecast of isolated cells in Hu et al. (2006) was largely dependent on the mesoscale features defined via the cloud analysis. Dawson and Xue (2006) found that model simulations initialized with and without use of a cloud analysis were able to forecast the presence of an MCS, although those using the cloud analysis did have superior forecasts of the event. Xiao and Sun (2007) also noted the increased accuracy of the model after several radar assimilation cycles. The impact of radar assimilation on storm spin-up time during the cycling period will be examined in this thesis.

1.4.2 Surface-based OSEs

Several studies have shown the importance of surface observations in creating accurate analyses and forecasts. Surface observations lack the high spatial resolution of radar observations, but they can provide coverage in the near surface area not observed

by any radar networks. Also, they generally provide a full set of model state information (temperature, wind, humidity), whereas radar data is most useful for the wind and precipitation information it contains, and the wind information, being just the radial component, is incomplete. Surface data assimilation has proven to be effective at improving accuracy of analyses of key mesoscale surface features in both 3DVAR and Ensemble Kalman Filter (EnKF) assimilation systems leading to more accurate predictions of weather phenomena across a wide range of scales. Mukhopadhyay et al (2004) found that the assimilation of surface observations during the monsoon season in India resulted in analyses that better captured the differential heating boundaries associated with terrain differences. The more accurate analyses generally led to more accurate rainfall estimation from the forecasts generated from these analyses (using equitable threat score and bias as a measure of QPF skill). For a squall line case over the southern plains of the United States, surface observations assimilated via EnKF resulted in more accurate frontal boundary strength and placement, leading to improved WRF model forecasts of squall line timing and storm structure (Ha and Snyder 2014). Precipitation forecast accuracy improved due to the better placement of these mesoscale features and the improved planetary boundary layer (PBL) representation. While the majority of improvement comes in the lowest levels where the surface observations are found, the low level observations were seen to have some effect on reducing error values at upper levels when compared to radiosonde soundings. The magnitude of positive impact on the upper levels is likely tied to the vertical correlation radius and would likely be more substantial in an EnKF system which uses an ensemble of

forecasts to predict the background error correlation matrix, including cross-correlations among variables.

An important part of data impact assessment is determining impact of one dataset in the context of other data types. Alapaty et al. (2001) found that surface observations improved the initial condition for an atmospheric boundary layer model. Importantly, they found the surface data impact was most pronounced when combined with assimilation of radiosonde data above the surface. This shows that in some cases surface data can be more useful when combined with other observation types to provide a complete description of the current atmospheric state. The following work will look for these types of relationships and optimal combinations of assimilated observation types from the multitude available within the DFW urban testbed.

One goal of this thesis is to address the impact of surface observations that are not currently widely assimilated operationally, including CWOP stations, AWS Weatherbug, and Understory sites. Further details on these observation networks are available in Chapter 2 of this work. Carlaw (2014) looked at the impact of CWOP, AWS Weatherbug, and Global Science and Technology (GST) Mobile Platform Environmental Data (MoPED) assimilated within the DFW testbed for ARPS simulations of a tornadic supercell from 15 May 2013 in Cleburne, TX. The thermodynamic observations from the Weatherbug stations in an area where there was a scarcity of conventional surface observations revealed more moisture in the lower levels. As a result, the subsequent model forecast had higher instability in the inflow source region. Subsequent increases in updraft velocity and vertical vorticity values, better matching the observed storm characteristics, were noted in the simulated storm

for the experiments that assimilated the Weatherbug temperature and dew point information. The impact of these non-conventional surface stations was also examined for hourly analyses in the north central Texas area over a month long period in March 2014. There was a clear dew point error reduction for the analyses averaged over the whole month when the non-conventional observations were assimilated. The study also notes the non-conventional observation assimilation results in improved accuracy of analyses of a cold front and dry line on separate days during the month long period. Interestingly, there was a degradation of the wind speed analysis when these observations were assimilated, likely due to poor siting of the non-conventional sensors. Comparisons of data denial experiment results from Carlaw (2014) and those in this study within a similar domain will be made, with the main differences likely to be attributed to the different forecast model used in the simulations.

1.4.3 ARW-WRF vs. ARPS Model

The WRF model has been chosen for this work, as it is used operationally by the National Center for Environmental Prediction (NCEP) in its two mesoscale models: the Rapid Refresh (RAP) model and the High Resolution Rapid Refresh (HRRR) model. Using this model setup should enable easier transition of conclusions to operational decision-making. From this study, the hope is to show how well the conclusions in Carlaw (2014), made using the ARPS model, could translate to the operational setting. This thesis aims to compare the results of forecasts from the ARPS model with those from the ARW-WRF model, looking for potential explanations for differences coming within each model's physical parameterizations or dynamical calculations.

Yan and Gallus (2016) used the ARW-WRF model with analyses generated from ARPS 3DVAR to show the value of high-resolution simulations in capturing convective storms more accurately. The better accuracy led to a higher skill score for QPF output. Improvements in convective-scale forecasts of thunderstorms would have substantial impact on hydrological forecasts of potential flooding impacts, as the main source of warm season QPF error is found in convective precipitation (Weisman et al. 2008). Radar assimilation has been shown to positively impact WRF model QPF associated with convective systems in several studies, despite a wet bias in the initial cycling period (Xiao et al. 2007; Moser et al. 2015). This thesis will continue looking at radar assimilation impact on QPF estimates with higher resolution forecasts than those used in these previous studies.

Knopfmeier and Stensrud (2013) used the ARW-WRF model to generate 5 km ensemble forecasts used in EnKF data assimilation for experiments looking at the effect of surface mesonet observations. Removing 75% of the mesonet observations did not result in substantial analysis degradation, which they believed was caused by the large background error correlation scales of the EnKF analysis. The ARPS 3DVAR system allows for multiple analysis passes resulting in the use of correlations scales that match more closely with the average observation spacing. Surface pressure observations have been shown to have a positive impact on analyses of pressure using EnKF data assimilation with the ARW-WRF model for cycling (Madaus 2014). The pressure observation assimilation only resulted in improvement to temperature and wind root mean square (RMS) error when those variables were assimilated from surface stations

as well. Assimilation of surface pressure tendency observations leads to similar RMS error reduction compared to analyses which assimilate surface pressure.

Aksoy et al. (2009) found substantial RMS error reduction by assimilating reflectivity and radial velocity radar observations into a cloud model version of the WRF, simplified from an operational version of the model. Assimilation of no precipitation radar observations was also used to effectively suppress spurious convection within the model domain. In creating the control experiment for the case presented here, spurious precipitation echoes were encountered in the initial trials. These were alleviated by adjusting several analysis and model parameters.

Recent studies looking at high resolution forecasts of tornadic storms, Carlaw (2015) and Stratman and Brewster (2015), both were able to reproduce observed rotation tracks with remarkable accuracy. The forecasts in these past studies used the ARPS model and generally had small track errors for the rotational center in the model compared to the observed tornado track. The work presented here also shows good predictability for the rotational elements of a tornadic supercell with the WRF model and ARPS 3DVAR data assimilation over a one hour and fifteen minute forecast period.

Chapter 2 will outline the details of the ARPS 3DVAR data assimilation and the ARW-WRF model used for the simulations in this study. Also, this chapter will more fully describe the observational data sets used and the pre-processing procedures performed on these data sets. A case study of a tornadic supercell in the Dallas area on December 26, 2015 will be the focus of chapter 3, including description of the synoptic setup, the experimental setup, and analysis results. The final chapter will discuss the

results and their implication within the context of similar research, along with suggestions for future research.

Chapter 2

2.1 Advanced Regional Prediction System (ARPS) Three-Dimensional Variational (3DVAR) Analysis Framework

The ARPS version of the three-dimensional variational analysis (Gao et al. 2004) method used here generates analyses to optimally fit the background forecast model and the observed variables. The scheme minimizes a cost function:

$$J(x) = \frac{1}{2}(x - x_B)^T \mathbf{B}^{-1}(x - x_B) + (H[x] - y_O)^T \mathbf{O}^{-1}(H[x] - y_O) + J_C \qquad (2.1)$$

Here x is the analysis state vector, x_b is the background state vector, y_o is the observation vector, $\mathbf{B}$ is the background error covariance matrix, $\mathbf{O}$ is the observation error covariance matrix, and H is a linearized forward operator which projects the model state to observation space. J_C is an additional penalty term in the cost function which is set to act as a weak anelastic mass divergence constraint.

$$J_C = \frac{1}{2}\lambda_C^2 D^2 \qquad (2.2) \qquad\qquad D = \alpha(\frac{\partial \bar{\rho}u}{\partial x} + \frac{\partial \bar{\rho}v}{\partial y}) + \beta\frac{\partial \bar{\rho}w}{\partial z} \qquad (2.3)$$

The penalty term, J_C, is shown in equation 2.2 with the divergence constraint D, shown in equation 2.3. λ_C is the weighting coefficient for divergence constraint, while D contains α (the horizontal weighting coefficient), β (the vertical weighting coefficient), and $\bar{\rho}$ (the mean air density at a given horizontal level). The anelastic mass divergence constraint acts to disperse observed radar radial velocities into the non-radial wind components (Gao et al. 2004; Hu et al. 2006b). It is a weak constraint meaning that the

anelastic continuity equation is not forced to be exactly satisfied which allows for retrieval of vertical motion fields. Carlaw (2014) uses a value of α that is an order of magnitude larger than the β based on Hu et al. (2006) which found that when the grid aspect ratio, Δx to Δz, is large (over 100) the finite differencing scheme creates an effect where the vertical wind component adjustment dominates the horizontal component adjustment. For this work, a stretched grid is used with horizontal grid spacing 20 times greater than vertical spacing near the surface but the horizontal and vertical weighting coefficients were set to the same value based on the Center for Analysis and Prediction of Storms (CAPS) DFW real-time forecast run for this case which produced an accurate forecast with this coefficient configuration.

In practice, a more efficient, incremental form of the cost function with preconditioning is minimized to obtain the analysis increments in the ARPS 3DVAR system. A first order recursive filter (Hayden and Purser 1995) is applied to create the Gaussian, isotropic spatial correlations in **B**. There is the option to apply multiple passes of the filter with different decorrelation length scales in each pass resulting in a different **B** matrix for different observation types. The **B** matrix does not include cross-correlations among different variable types and all observation errors are assumed uncorrelated such that **O** becomes a diagonal matrix. Gao et al. (2004) contains further details on the ARPS 3DVAR analysis system.

2.1.1 Incremental Analysis Updating (IAU)

Incremental Analysis Updating (IAU) is a technique used during the assimilation period in this work. It has been shown to reduce the spurious noise that can result from

forcing the model to adjust to a large amount of new information being introduced all at the initial time (Brewster 2003). This method, described in Bloom et al. (1996), applies the analysis increments generated at the initial time as a forcing term for the model over a specified time window at the beginning of the simulation period. The IAU equation is shown below (Equation 2.4),

$$\frac{dX(t)}{dt} = F(X) + \alpha_{IAU}(X_a - X_b) \quad (2.4)$$

where X is the model variable, F represents the model forcing terms, and α_{IAU} is the weighting coefficient multiplying the analysis increment, $(X_a - X_b)$. The increments are applied at regular intervals during the large time step after the other forcing terms. In these experiments the fractional increments are applied in a triangular shape over the time interval such that the maximum fraction of the increment is applied in the middle of the time window. There is also now the ability to apply variable dependent timing for the increments with wind and latent heat variables being applied asymmetrically toward the beginning of the time window and hydrometeor variable increments being biased towards the end of the time window. This results in better establishment and maintenance of thunderstorm updrafts with hail, graupel, and heavy precipitation as shown in Brewster et al. (2015). Vertical velocity and pressure increments are not used in the IAU process in this work because these variables quickly respond to changes in other fields at storm scales. More information on the IAU implementation in ARPS can be found in Brewster (2003).

2.1.2 Complex Cloud Analysis

Rather than variationally assimilating reflectivity, which is made difficult by the non-Gaussian error distributions for such fields while there exist fairly straightforward direct relationships between observed reflectivity and the hydrometeor fields in the model, the ARPS complex cloud analysis is used. After the minimization step in ARPS 3DVAR, the cloud analysis uses radar, satellite, and surface data to adjust the hydrometeor mixing ratio fields based on inverting relationships for computing reflectivity from the hydrometeors and common sense physical rules based on temperature, etc (e.g., Ferrier 1994; Rogers and Yau 1989).

Background hydrometeor field values are supplanted by the cloud-analysis based hydrometeor fields wherever reflectivity observations are present, and zeroed-out where there is radar coverage and below-threshold reflectivity. The relative humidity is set below saturation where such rainfall is removed. In cycled mode, the background values are used to define the ratios among the reflectivity factors contributing from the various hydrometeor species. All the effects of spurious precipitation echoes within the model background (such as latent heat bubbles) are difficult to remove without complex and very expensive EnKF cross-correlation calculations (Xue et al. 2013a). The North American Mesoscale (NAM) model, which lacks explicit convection, is thus well suited to use as a background field for this method.

In addition to modifying the hydrometeors, the cloud analysis applies an increase in temperature within a precipitating cloud. Latent heat release is accounted for by implementing a moist adiabatic ascent profile from cloud base and adjusting the background upward in areas of active convective updraft where it is less than this

profile. More information on the cloud analysis procedure and latent heat adjustment can be found in Carlaw (2014), Brewster et al. (2005), and Hu et al. (2006).

2.1.3 Radar Remapping

Three different types of radars are assimilated in this work and these require a pre-processing step. In order to assimilate the raw level-II radar data into ARPS 3DVAR it is necessary to interpolate the data from the native polar coordinate of the radar to the Cartesian, terrain-following ARPS grid used for the analysis. The pre-processing procedure also involves several quality control checks. Anomalous propagation is identified in areas where there are large vertical reflectivity gradients coincide, low correlation coefficient and/or near-zero radial velocities. Radial artifacts from blockages or radiation interference from the sun are removed. Any transient isolated echoes determined to be from non-meteorological scatterers are also removed via a "despeckling" algorithm. There is also a velocity de-aliasing procedure where radial velocities are first subtracted from a background wind field. This allows isolated areas of folded velocities to become more apparent during horizontal consistency checks across adjacent radials, which is done following the Eilts and Smith (1990) de-aliasing procedure applied sequentially in the clock-wise and counter-clockwise direction. The quality-checked data is then interpolated to the ARPS grid via a local least squares fit to a quadratic function in the horizontal and a linear function in the vertical. Output options include reflectivity, radial velocity, and Velocity Azimuth Display (VAD) wind profiles. A more detailed description of the ARPS radar remapping procedure can be found in Brewster et al. (2005).

2.2 Modeling

2.2.1 Advanced Research Version of the Weather Research and Forecasting Model (ARW-WRF)

The WRF model is designed to be a community mesoscale model for both operational and research-based applications. Development of the WRF model has been a joint effort between several different government and academic entities in order to facilitate easy transfer of research conclusions to the operational framework (Skamarock et al. 2008). It has been used to evaluate convective-scale QPF skill (Yan and Gallus 2016; Moser et al. 2015), simulate tropical cyclones (Cha and Wang 2013), and tornadic supercells (Clark et al. 2012).

This work uses version 3.6 of the ARW-WRF for the free forecast period simulations. The ARW solver uses fully compressible, Euler non-hydrostatic equations with conservative scalars. A terrain-following, hydrostatic pressure vertical coordinate called η is utilized with vertical stretching capability and a constant pressure model top at 50 hPa. The horizontal grid is a staggered Arakawa C-grid and the time step can be 2nd or 3rd order Runge-Kutta. Nesting capability is also available. The WRF Preprocessing System (WPS) is used to set up the initial and boundary conditions necessary to run the WRF model. There are four programs that would usually need to be run prior to the WRF simulation. The first defines the geographical fields within the simulation grid. The next one unpacks the Gridded Binary (GRIB) data from the external model used. The third step interpolates this unpacked data onto the three-

dimensional WRF grid. The final pre-processing step then creates the initial condition and external boundary condition files necessary to run the main WRF executable. For this work, the initial and external boundary conditions come from data on the ARPS grid. The program ARPS4WRF is used to interpolate the data onto the WRF simulation grid, replacing the second and third pre-processing steps in WRF described above.

2.2.2 ARPS model

The ARPS model is used to produce the ten-minute forecasts during the cycled data assimilation period in this work. The IAU increments are applied within this window. ARPS was originally developed at CAPS at the University of Oklahoma in the early 1990s. It is a regional forecast system capable of storm scale simulations used for operational, commercial, and research applications throughout the meteorological community. ARPS has been used to simulate a wide range of weather phenomena including tornadoes (Xue et al. 2014), tropical storms (Zhao and Xue 2009), and MCS events (Dawson et al. 2006). It is a three-dimensional compressible, non-hydrostatic model with a generalized terrain-following vertical coordinate on an Arakawa C-grid. User-specified stretching is available for the vertical coordinate. The second-order leapfrog scheme is used for large time step discretization with an Asselin time filter option.

2.3 Observations and Quality Control

2.3.1 Conventional observations

In each experiment carried out here, observations from conventional sources are assimilated. The data sources deemed to be conventional for this case are any observation types currently included in the federal observing network for assimilation into operational NWP models. One of these is the Automated Surface Observing Station (ASOS) network, which is the primary surface observing network for the United States. The ASOS network was brought about by the NWS, the FAA, and the Department of Defense (DOD) to provide vital information for aviation operations, forecast applications, and weather and climate research (NWS 1999). A similar network consists of the Automated Weather Observing System (AWOS) stations, which make up an older, FAA-based network reporting data at 20-minute intervals. There are also several conventional surface mesonets, including the Oklahoma Mesonet and the West Texas Mesonet, which provide enhanced resolution of surface meteorological conditions in the respective regions. Upper air information is provided via the Aircraft Communications Addressing and Reporting System (ACARS), which relays flight level temperature, dew point, and wind information for use in NWP models (NWS 2006). Also, NWS-launched radiosonde profile information is assimilated whenever available. The currently available national network of WSR-88D NEXRAD radars is also utilized to look at the baseline impact of the current radar network. The most prominent NEXRAD radar in this area is the one at Fort Worth, Texas. Any NEXRAD radar

whose domain intersects the model domain is also used, so there are a total of 7 radars in the NEXRAD data set for this work.

2.3.2 Non-conventional observations

There are several available data sets that are not currently assimilated into the operational NWP models. One of these datasets is the Automatic Position Reporting System as a Weather Network (APRSWXNET), which is made up of over 10,000 amateur surface observers relaying information from weather stations at a diverse set of locations to the Meteorological Assimilation Data Ingest System (MADIS) (CWOP 2014). Another dataset not operationally assimilated whose impact will be assessed for the case studied here is the Automated Weather Services (AWS) WeatherBug network. Operated by EarthNetworks, it consists of weather stations located mostly near schools and broadcast stations. Its original purpose was to provide local weather information for weather broadcasts and also to form a basis for meteorological curricula within schools. With over 8,000 stations over a wide range of locations there is tremendous potential utility of the observations for NWP forecasts and research purposes (NOAA 2004). Also, many of the Weatherbug stations are located near emergency-response facilities and are used to aid in situational awareness and enable more informed decision-making from emergency responders (Hicks et al. 2012). The third non-conventional surface observing network examined is the relatively newly developed set of weather stations from Understory Weather. Understory has deployed a network of sensors in the immediate Dallas area which can detect hail, rain, and wind in three

dimensions as well as moisture and temperature information. These data are designed to be used by insurance companies to better respond to weather events, as well to improve weather forecasts from NWP models (Understory 2016). These three surface observing networks do not follow the same strict siting standards that the ASOS/AWOS stations are required to meet. As a result, there is the possibility of a lack of representativeness and potential for bias in the observations obtained at these stations. These errors can be accounted for in the data assimilation process and any gross instrument errors are likely to be captured within the MADIS quality control check performed for each of these data types or the quality control checks within the ARPS 3DVAR pre-processing. It is clear that more care is required when working with these datasets, but there is potential utility to assimilating these observations as has been shown in Carlaw (2014).

Other non-conventional observation types specifically available within the DFW testbed include the 8 X-band radars (7 of which have been installed and are operational at this time), 3 radiometers, and 2 SODARs. The Radiometric microwave radiometers (MWRs) are supplied by EarthNetworks. These instruments are able to retrieve a vertical profile of temperature and dew point within the troposphere via conversion of observed brightness temperatures using the radiative transfer equations (Lundquist et al. 2016). These profiles are potentially useful for their ability to augment the information provided by the radiosonde soundings by adding additional locations where vertical profiles are available and by providing a continuous data stream. Radiosonde data is only available every twelve hours (occasionally 6 hours) and the radiometer data provides information within this time gap where no other vertical thermodynamic

profiles would be available within the current federal observing system. Unfortunately, the inclusion of the radiometer data resulted in pronounced differences in the forecast/analysis fields in this work likely due to cloud effects on the radiance observations not accounted for in the assimilation system. More information on the problems with the radiometer data assimilation can be found in Appendix A.2.

In order to provide a continuous vertical profile of the horizontal wind, two WeatherFlow SODARs (one at the NWS forecast office in Fort Worth and another in Midlothian, TX) were installed. These SODARs provide similar information to the former Doppler wind profiles that had been part of the now defunct national wind profiler observation network (Unidata 2014). These instruments are able to derive wind speed and direction based on the Doppler shift of sonic pulses reflecting off atmospheric temperature gradients (Land and Mckeogh 2011). The SODARs and radiometers in the network complement each other as one has thermodynamic profile information and the other has dynamic profile information. Together they provide the same type of datasets as a radiosonde but at much higher temporal frequency. Experiments presented here will look at the impact of available SODAR data.

Finally, the DFW urban testbed currently includes a network of seven operational X-band radars, some of which were provided by CASA and others which were provided by various private sector companies. These radars provide enhanced spatial coverage within the immediate DFW metro area as well as faster update speeds compared to that available from the WSR-88D radar in the area. The closely-spaced radars allow for a more complete sampling of the lowest levels of the atmosphere where key storm-scale processes often go unobserved. The storm studied in this work is approximately 80 km

away from the KFWS radar when it produces a tornado and so even the 0.5° elevation beam is above 2 km in this scenario. To see how the CASA radar data can fill in information in this gap in radar coverage, this work examines the impact from assimilating the data from all radars and then from individual radars, especially those in closest proximity to the event of interest. There are also 2 TDWR radars available for assimilation at the two major airports in the DFW area. These are 5-cm wavelength radars which provide enhanced wind shear and precipitation detection capabilities close to airports primarily for aviation applications. These radars are only present in select regions of the country and in this work their impact will be examined and compared with the impacts of the other radar types. The spatial distribution of radars assimilated in this study can be seen in Figure 2.1a and a typical distribution of surface observations assimilated in the experiments carried out here can be seen in Figure 2.1b.
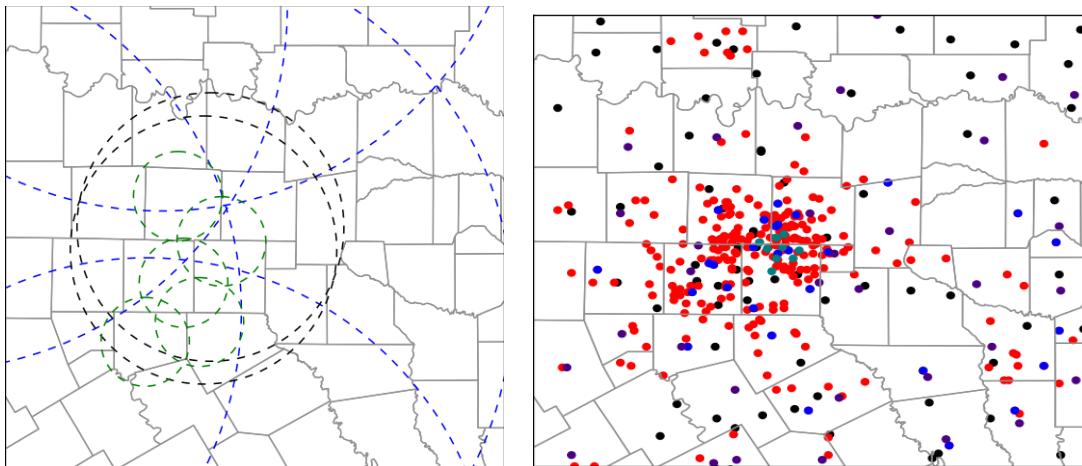
Figure 2.1: a) Radar range rings for the three types of radars assimilated here (TDWR, CASA, and NEXRAD) and b) observation locations for the conventional and non-conventional surface observation types assimilated at the final analysis time (2345 UTC).

2.3.3 Quality control procedures

Several of the observation types assimilated in this work are obtained from the Meteorological Assimilation Data Ingest System (MADIS) and these datasets are internally monitored using quality standards outlined in the NWS Techniques Specification Package (NWS 1994). Various data-checking is also implemented on the radar data via the methods described in the previous section on the ARPS radar remapper.

Within the ARPS3DVAR program there are several quality control steps checking for erroneous observations. Observations are compared to a local Barnes (Barnes 1964) analysis of the surrounding observations to each observation location to ensure that there is spatial consistency among observations in proximity to each other. Another component is the temporal consistency check which compares observations at the same location from subsequent times looking for the change in observed value over that time interval. Anytime the difference between the observational value and its counterpart exceeds a certain difference threshold the observation is deemed to be unreliable and is not used within the assimilation at that time. The observation is also compared to the interpolated background value at that observation location. Again, deviations of the observation from corresponding background values larger than a specified threshold are discarded before the minimization procedure is called. Finally, there is a check for low wind speed biases due to siting issues (locations sheltered by trees and/or buildings) that can be prevalent with the non-standard observations assimilated here. The procedure is drawn from Carlaw (2014), and it involves discarding any wind speed observations that are less than 1 ms^{-1}, when the corresponding background wind speed value is greater than 5 ms^{-1}.

Chapter 3

3.1 Case Study

3.1.1 Event Details

One of the most significant tornado outbreaks in the history of the north central Texas area occurred on 26 December 2015. This event was notable for its substantial societal impact and the unusual time of year during which it occurred. There were a total of 12 tornadoes in 8 counties in the region. One of the supercell thunderstorms on this day produced an EF3 tornado that went from northwestern Ellis County to southern Dallas County through the towns of Midlothian, Ovilla, and Glenn Heights from 0000 UTC to 0015 UTC causing extensive damage to several homes, two churches, and an elementary school. This storm will be referred to as the Ovilla storm in this text and will be identified with a red circle around it in several of the figures.

This study focuses on simulating the strongest and most impactful storm of this event which initiated in central Ellis County and went on to produce a series of tornadoes, including an EF4 tornado, beginning in northeastern Dallas County at 0045 UTC and ending in Rockwall County at 0100 UTC. This storm will be referred to as the Rowlett storm in this text and will be identified with a black circle around it in the figures which include it. There were 10 fatalities caused by the Rowlett EF4 tornado with majority of these occurring as the circulation moved directly over the intersection of the President George W. Bush Turnpike and U.S. route 67, an area with heavy traffic just southeast of Rowlett (Figure 3.1). The interaction and eventual merger of the

Rowlett storm with the Ovilla storm results in a complex forecast scenario where an accurate initial state estimate is likely critical to producing an accurate model forecast.
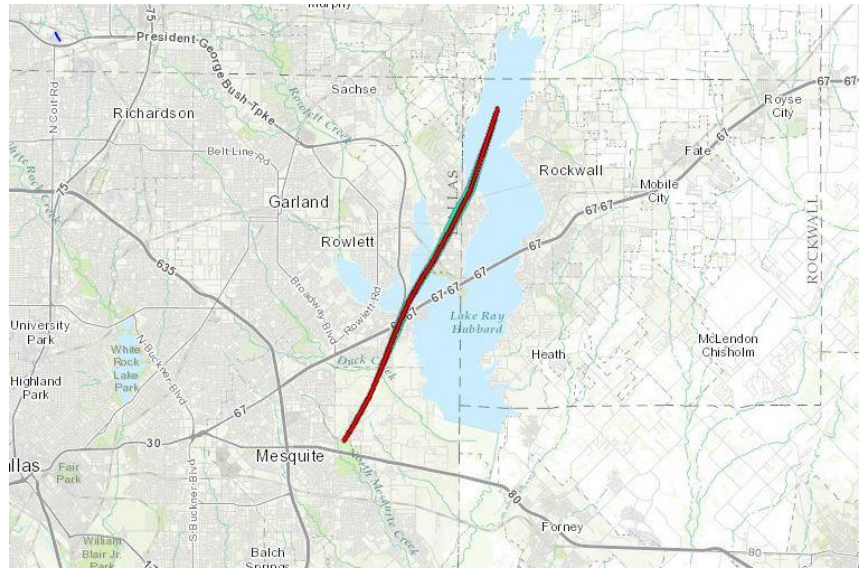
Figure 3.1: Estimated damage path of Rowlett tornado from northeast Dallas County to northwestern Rockwall County (image taken from the NWS damage assessment toolkit page https://apps.dat.noaa.gov/StormDamage/DamageViewer/)

3.1.2 Synoptic Setup

A trough at 500 hPa centered over southern California at 12Z on 26 Dec 2015 moved south and east towards northern Mexico throughout the day (Figure 3.2). At the surface, a warm front draped from Wichita Falls, TX eastward to just north of Texarkana, TX (evident in the equivalent potential temperature field in Figure 3.3a) slowly progressed north throughout the morning hours of the 26th. Elevated storms developed in the warm advection regime north of the front with isentropic ascent associated with a strong southerly low-level jet seen in Figure 3.4. A surface low in northeastern Mexico slowly shifted east throughout the day. By 18Z, a cold front from the southern high plains advanced rapidly southeast into north central Texas (Figure 3.3b). Mid-level lapse rates of around 7 Kelvin per km combined with strong surface

heating led to 1500-2000 J/kg of surface-based convective available potential energy (CAPE) with minimal convective inhibition (CIN) across the warm sector in north-central Texas (Figure 3.3c). Strong directional shear developed in the lower levels to the south and east of the front with southeasterly winds at the surface and 40-50 knot southerly winds at 850 hPa over the region. This contributed to the development of widespread areas of 200 m^2/s^2 storm relative helicity (SRH) in the lowest kilometer of the atmosphere and supercell composite parameter (SCP) (Thompson et al. 2003) values between 8 and 12 (Figure 3.3d). The values for these parameters as well as the sounding from this day (Figure 3.5) indicate the potential for severe weather with any storm in the area. Upper level forcing for ascent was still displaced well to the west during the afternoon so the storm coverage was isolated throughout the day. The isolated storms that did develop were in an environment favorable for rotating supercells, several of which ended up producing tornadoes.
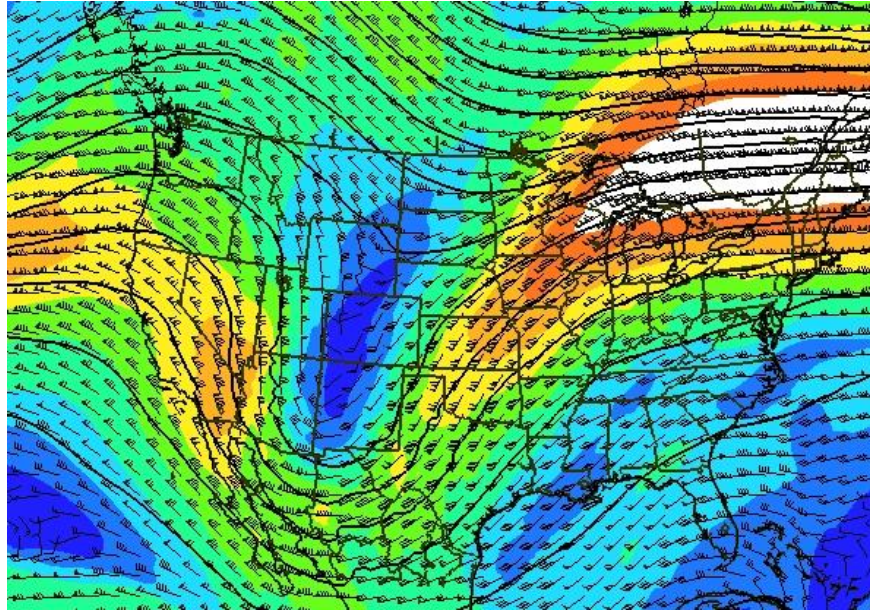
0000 UTC Dec 27 2015

Figure 3.2: 6-hour NAM forecast of 500 hPa height (black contours), wind speed (kts) (color fill), and wind vectors at 00 UTC on 27 December 2015.
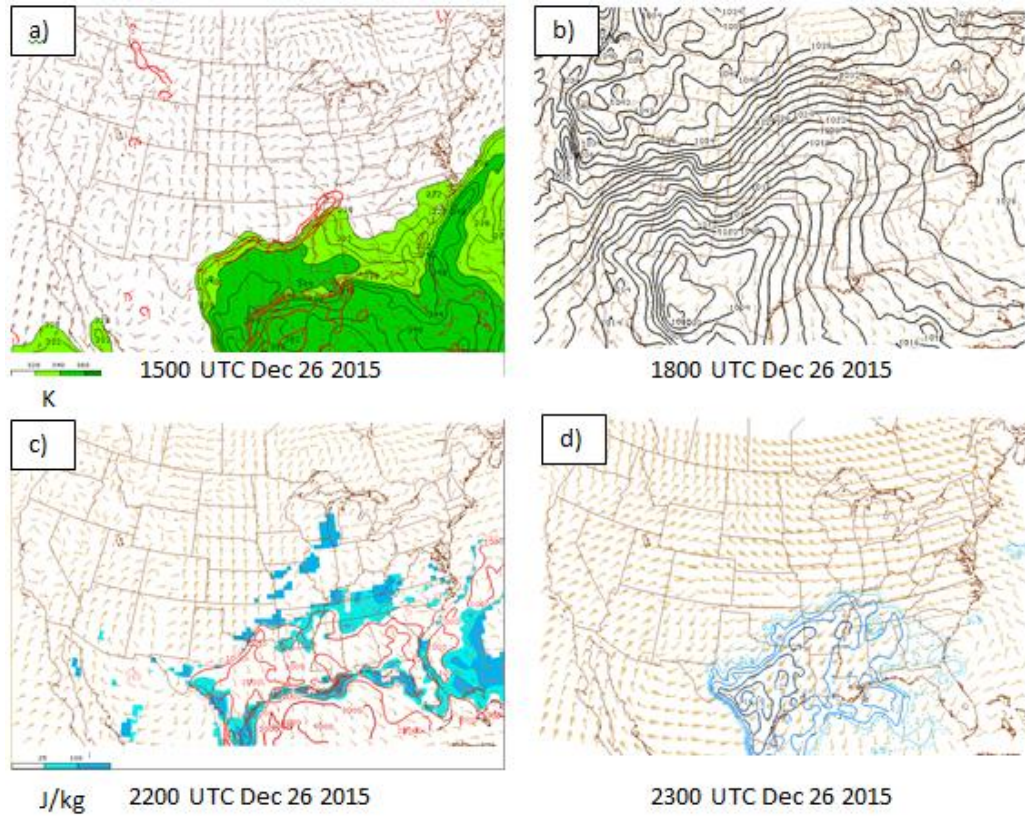
Figure 3.3: a) Theta-e (color contour) and Theta-e advection (red contour) with surface winds at 1500 UTC 26 Dec 2015, b) mean sea-level pressure (MSLP) and surface wind at 1800 UTC 26 Dec 2015, c) Surface-based convective available potential energy (red contour) and convective inhibition (blue color contour) at 2200 UTC 26 Dec 2015, and d) supercell composite parameter with Bunkers storm motion (kts) at 2300 UTC 26 Dec 2015.

1800 UTC Dec 26 2015
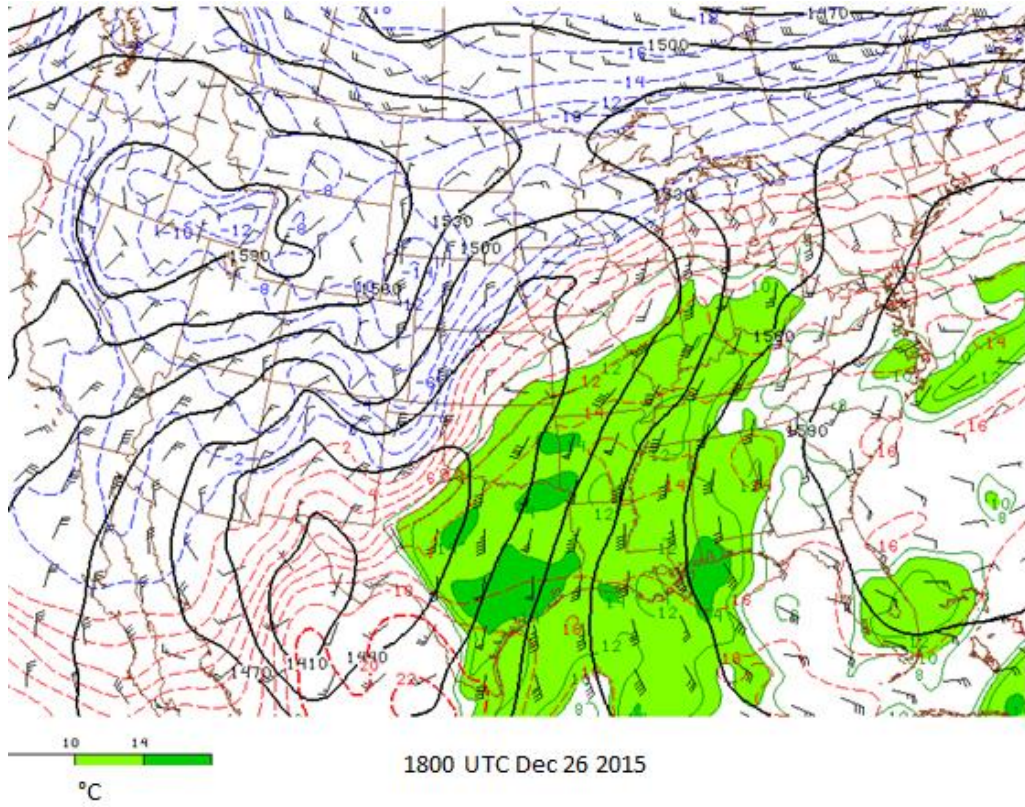
Figure 3.4: 850 hPa height, wind speed (kts), and dewpoint (green color contours) at 1800 UTC on 26 December 2015.
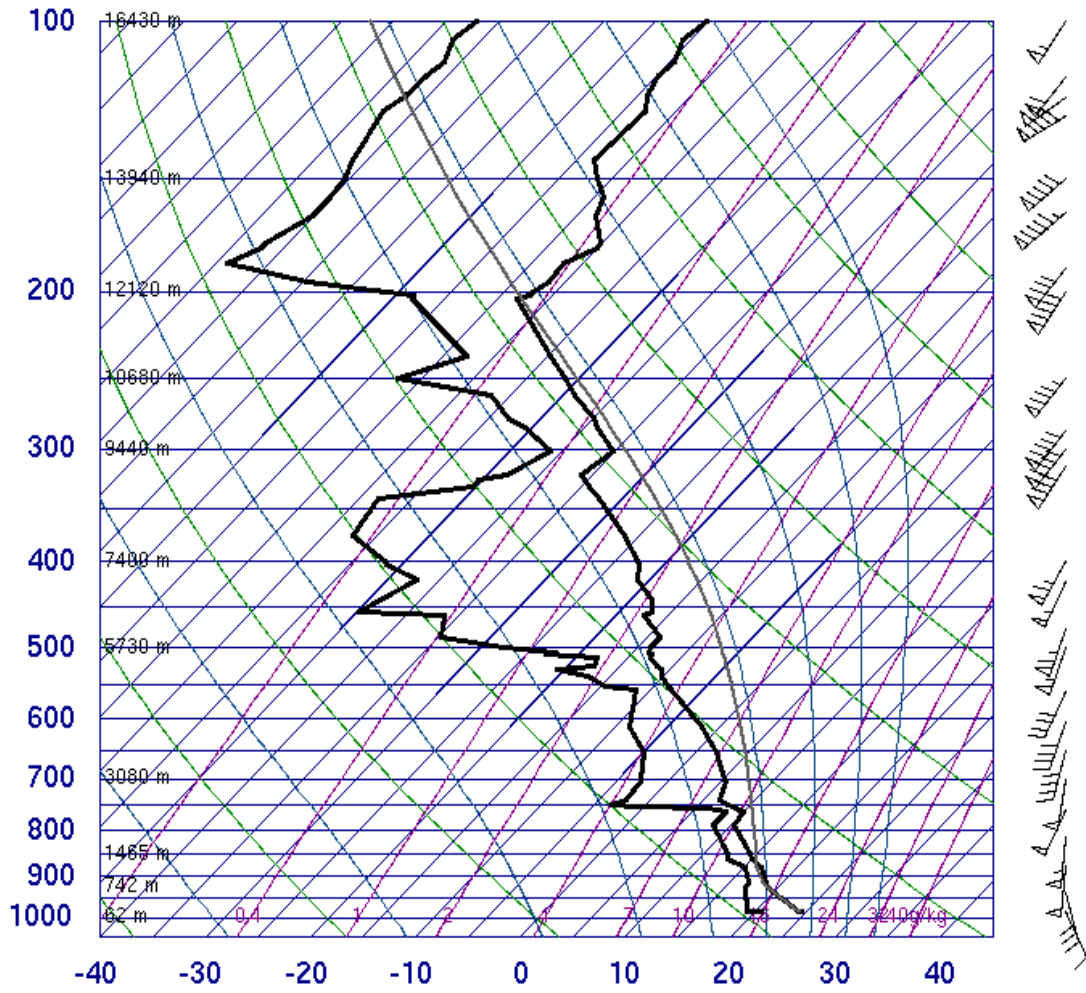
Figure 3.5: Observed sounding from NWS Fort Worth at 1800 UTC on 26 Dec 2015.
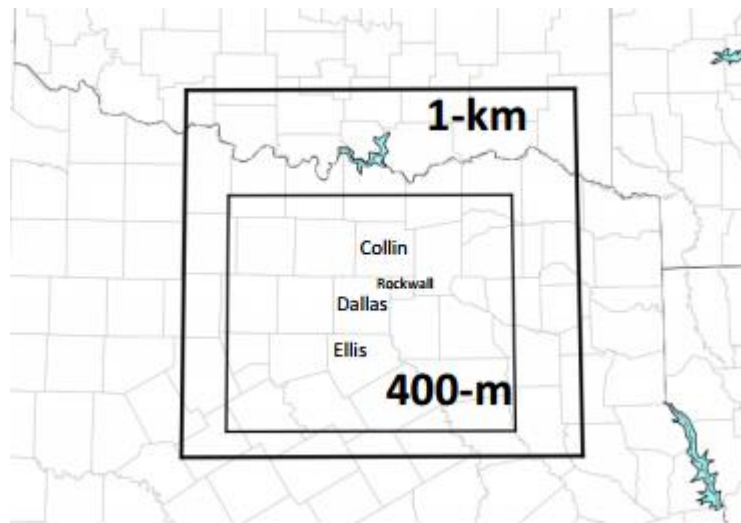
Figure 3.6: Depiction of the 1 km outer domain and the 400m inner domain centered on the Dallas metro area. Selected county names addressed in this work are also displayed.

3.2 WRF model grid setup and specifications

For the experiments run here, a larger outer ARPS grid with 1 km horizontal grid spacing is used for the 10-minute data assimilation cycling period. A smaller, higher resolution (400 m grid spacing) inner grid is then used for the WRF simulations during the free forecast period. The outer grid specifications are the same as those used in the CAPS real-time forecast system, which had an accurate forecast of the rotation associated with the Rowlett tornado for this case. More information on the real-time forecast and analysis configuration can be found in Brewster et al. (2014). The 400 m domain is reduced in size in order to facilitate reasonable computational times for the higher horizontal resolution. The outer domain is centered at 33° N, 96.5° W and is about 360 km x 320 km. The inner domain is centered at 32.65° N, 96.7° W and is approximately 240 km x 208 km in size (Figure 3.6). The vertical grid spacing is non-uniform, with more grid levels closer to the ground and increased grid spacing between

the higher levels of the model. The vertical grid spacing is 20 m at the lowest model level and follows a hyperbolic tangent function (Xue et al. 1995) increasing to 400 m at model top, with a total of 53 vertical levels for both domains. ARPS surface data files are used to establish the land surface features in the model, with the 30-second US Geological Survey (USGS) terrain dataset used to establish the model terrain elevation field for both grids. For the ARW-WRF forecasts run here, the microphysics scheme used is the single-moment Lin et al. (1983) scheme, the radiation parameterizations used are the Goddard shortwave scheme (Chou and Suarez 1994) and the Rapid Radiative Transfer Model (RRTM) longwave scheme (Lacono et al. 2008). The 1.5 TKE turbulence closure scheme is also utilized along with the Noah land-surface model for surface physics (Tewari et al. 2004). The lateral boundaries for this free forecast are forced by the 18 UTC NAM forecast field.

Table 3.1: Data assimilation combinations for the data impact experiments.

Experiment	Conventional surface data	Non-conventional surface data	CASA data	88D data	TDWR data	Upper air profiles
CTL	All	All	All	All	All	All
NOCASA	All	All	None	All	All	All
NO88D	All	All	All	None	All	All
NOTDWR	All	All	All	All	None	All
NONEWSFC	All	None	All	All	All	All
NONEW	All	None	None	All	None	Raob and 88d VAD profile
NOCASAVR	All	All	Reflectivity data only	All	All	All
NOMDL_NOUTA	All	All	XUNT,XICO, and XADD only	All	All	All
NOVR	All	All	Reflectivity data only	Reflectivity data only	Reflectivity data only	All
NOSODAR	All	All	All	All	All	Raob and VAD profiles only
NORADAR	All	All	None	None	None	All

3.3 Experimental design

The cycled assimilation of different sets of observation types for each experiment is performed on a 1 km ARPS grid in order to incorporate the IAU scheme, which worked successfully in the ARPS real-time runs, but does not have a readily-available WRF equivalent. The initial conditions for the first assimilation cycle at 2335Z were obtained from the 5 and 6 hour forecasts from the 18Z NAM model interpolated to this intermediate time. The set of observation types for each experiment, detailed in Table 3.1, were assimilated via ARPS 3DVAR on the 1 km grid at the initial time. A 10-minute ARPS forecast was then run from this analyzed state with boundary forcing every 5 minutes from the NAM model forecast. Specified input values for this ARPS forecast can be found in appendix A (Table A.1). A final analysis is obtained at 2345Z, and this is interpolated down to 400m and converted to the WRF model grid format via ARPS4WRF. This field is then used as the initial condition for the 400 m WRF free forecast run from 2345Z to 0100Z. A schematic of the assimilation procedure is shown in Figure 3.7.

The main focus of this work is to assess the impact of the additional radar data present in the DFW testbed, so a majority of the experiments focus on denial of radar data. There is one experiment which focuses on the effect of non-conventional surface data, such as Weatherbug and CWOP stations, similar to the work done by Carlaw (2014) with the ARPS model. The CTL experiment includes assimilation of radial velocity and reflectivity data from the NEXRAD WSR-88D, CASA, and TDWR radars covering the domain. It also includes the NWS Fort Worth radiosonde profile from the available radars, surface data from ASOS/AWOS stations, higher quality conventional

surface networks (West Texas and Oklahoma Mesonets), non-conventional surface sources such as Weatherbug, CWOP, and Understory, and individual ACARS aircraft observations. The NOCASA experiment is the same as the CTL experiment except the radial velocity and reflectivity data from the five CASA radars in the domain at this time are denied. NONEWSFC denies Weatherbug, CWOP, and Understory surface data from being assimilated. Similar to the NOCASA experiment, NO88D and NOTDWR deny observations from those respective radar networks. NOCASAVR denies only the radial velocity from the CASA radars, still using the reflectivity data in the complex cloud analysis. In order to look into the effects of the location of the different CASA radars relative to the Rowlett storm, the closest CASA radars at the time of assimilation were denied in another experiment (NOMDL_NOUTA). The NONEW experiment, with conventional data only, was run to get an idea of what the baseline performance of the model forecast would be in a typical observing system scenario without the additional data types present in the DFW Urban Testbed.

1-km Domain (10 min assimilation cycle)

2335   2345

IAU increments
applied   0100

400-m domain ────────────────────→

(1-hour 15 min forecast)
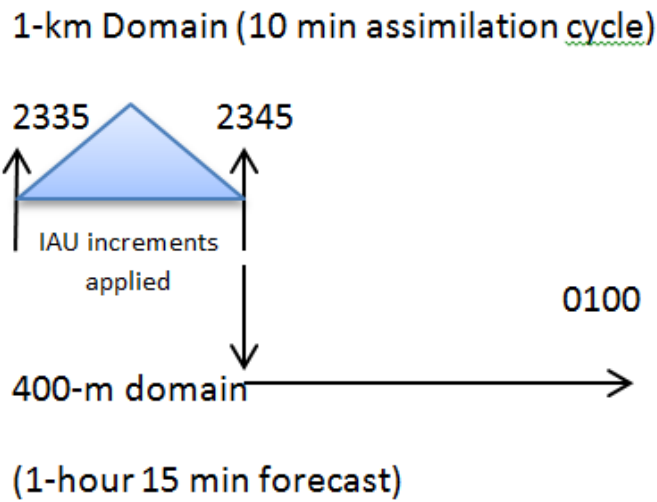
Figure 3.7: Assimilation procedure for the experiments presented here. ARPS forecast run from 2335 UTC to 2345 UTC and a WRF forecast from 2345 UTC to 0100 UTC. Lateral boundary conditions come from the 12 km NAM model.

The ARPS 3DVAR system allows for multiple passes to account for the varied observation spacing among observation types. A different radius at which the observational increment correlation becomes e-folded (decorrelation length scale) can be used for each new pass. For these experiments the ASOS/AWOS, high-quality mesonet, ACARS, and radiosonde data are assimilated on the first pass with decorrelation radius of 45 km as these datasets are representative of a fairly widespread region. The second pass includes the remaining, more dense data assimilated using a smaller horizontal decorrelation radius of 2 km to fill in small-scale details not captured by the first set of observations. The vertical decorrelation radius is specified as 4 grid points for both passes of the recursive filter.

3.4 Results

The following section presents notable findings from the set of OSEs carried out in this work. Storm features such as associated reflectivity field and rotational characteristics are compared across experiments. Rainfall/flash flood prediction impact is assessed by qualitatively comparing the model-generated accumulated rainfall estimates from each experiment to the observed accumulated rainfall field. Finally, we discuss significant differences in the low-level thermodynamic fields in a portion of the domain stemming from the inclusion of non-conventional observations.

3.4.1 Reflectivity comparison

Comparing the CTL experiment 1 km above ground level (AGL) reflectivity (Fig. 3.8a) at the final analysis time (2345 UTC) to the observed reflectivity on the 0.5° tilt from the KFWS NEXRAD radar (Fig. 3.8e), the CTL reproduces the observed reflectivity field accurately with slight differences in magnitude of reflectivity values in some of the convective elements. Many of the other experiments presented here, including the NOCASA run (Fig. 3.8b), show a similar analyzed reflectivity field with some slight differences from the CTL field and overall good agreement with the observed reflectivity. The modeled reflectivity values (thresholded at 20 dBZ) are derived from model hydrometeor mixing ratio values using equations specific to the Lin microphysics scheme used here. The two experiments with noticeably different reflectivity fields are NO88D (Fig 3.8c) and NORADAR (Fig. 3.8d). The NORADAR experiment has no simulated reflectivity present at the final analysis time as the model takes about 15 minutes to "spin up" a coherent precipitation field without assimilation of radar data.
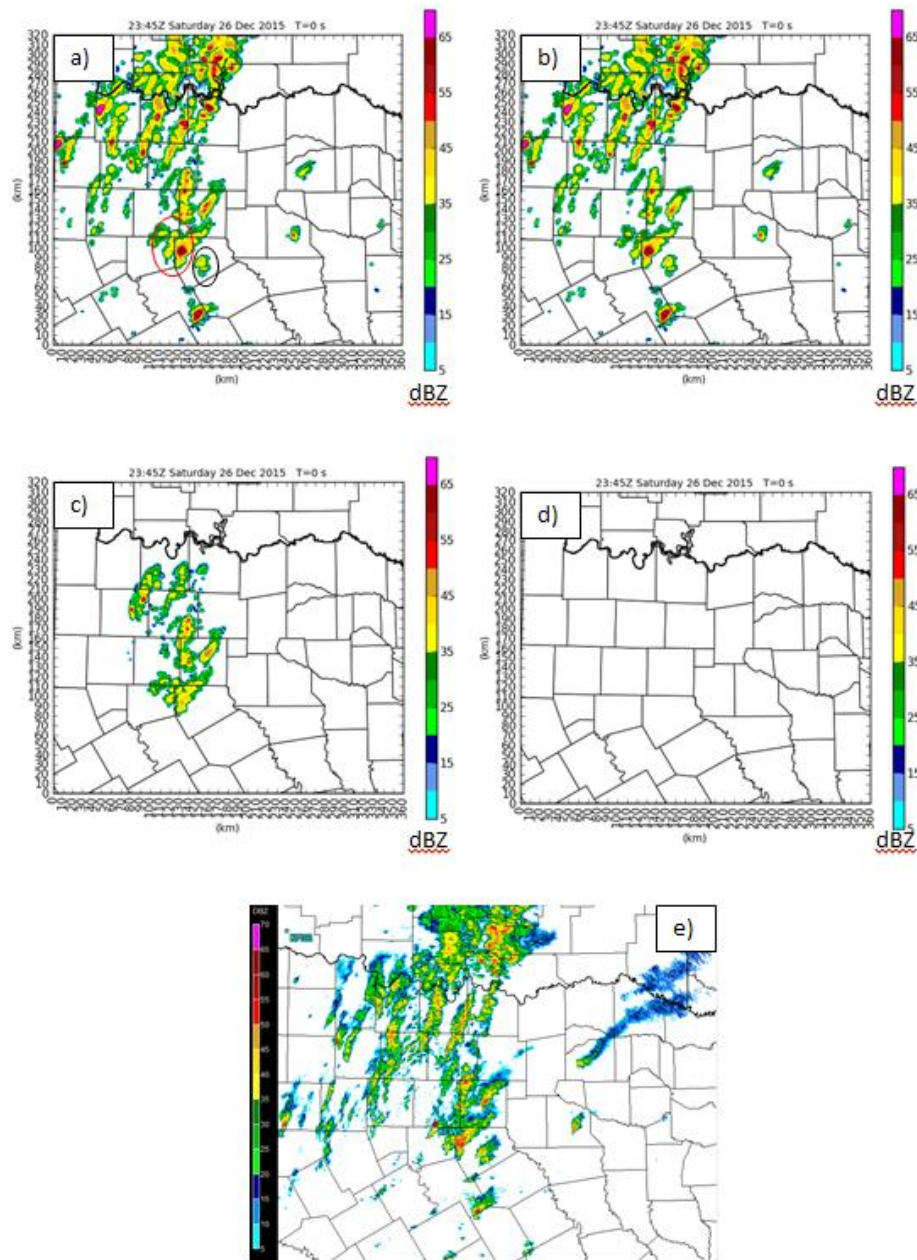
Figure 3.8: 1 km AGL reflectivity field at final analysis time (2345 UTC) for experiment a) CTL, b) NOCASA, c) NO88D, d) NORADAR, and e) observed KFWS 0.5° elevation angle. The Rowlett storm is circled in black while the Ovilla storm is circled in red.
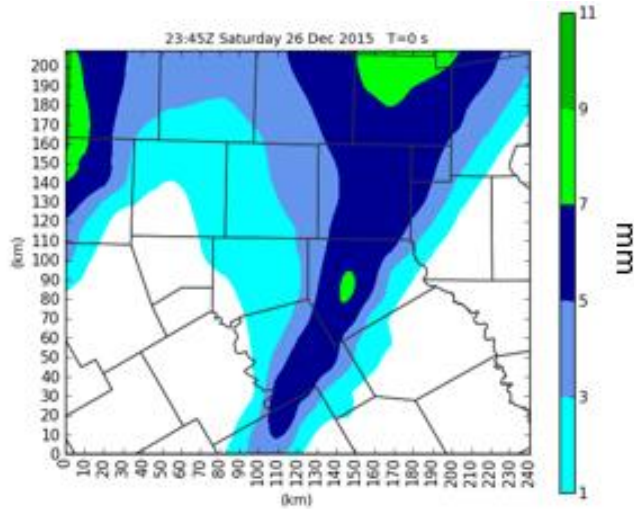
Figure 3.9: Model accumulated QPF in the background field for the NORADAR experiment at 2345 UTC.

The background field used does have some large-scale precipitation areas at this time, (Fig. 3.9) but it does not contain information on the hydrometeor mixing ratio values which are needed for the reflectivity calculations. Also, the NO88D experiment (Fig. 3.8c) shows a similar effect with missing reflectivity in the areas where the only radar coverage is provided by the more expansive range of the WSR-88D radars. In these two experiments, the reflectivity field associated with the developing supercell in central Ellis County is not properly analyzed. This is the storm that goes on to produce the Rowlett tornado and its inaccurate initialization in these two experiments leads to a much poorer forecast of its development and subsequent rotational characteristics.

Looking at the 45 minute forecast valid at 0030 UTC on 27 December 2015 (Figure 3.10), the overall reflectivity field is generally weaker in the NORADAR experiment (Fig. 3.10c) than the CTL experiment (Fig 3.10a) for the convective storms within the domain. The CTL experiment does seem to be suffering from a wet bias in the model

with a much greater area of 50 dBZ or greater reflectivity compared to the observed reflectivity from KFWS over the domain at this time (Fig. 3.10d).
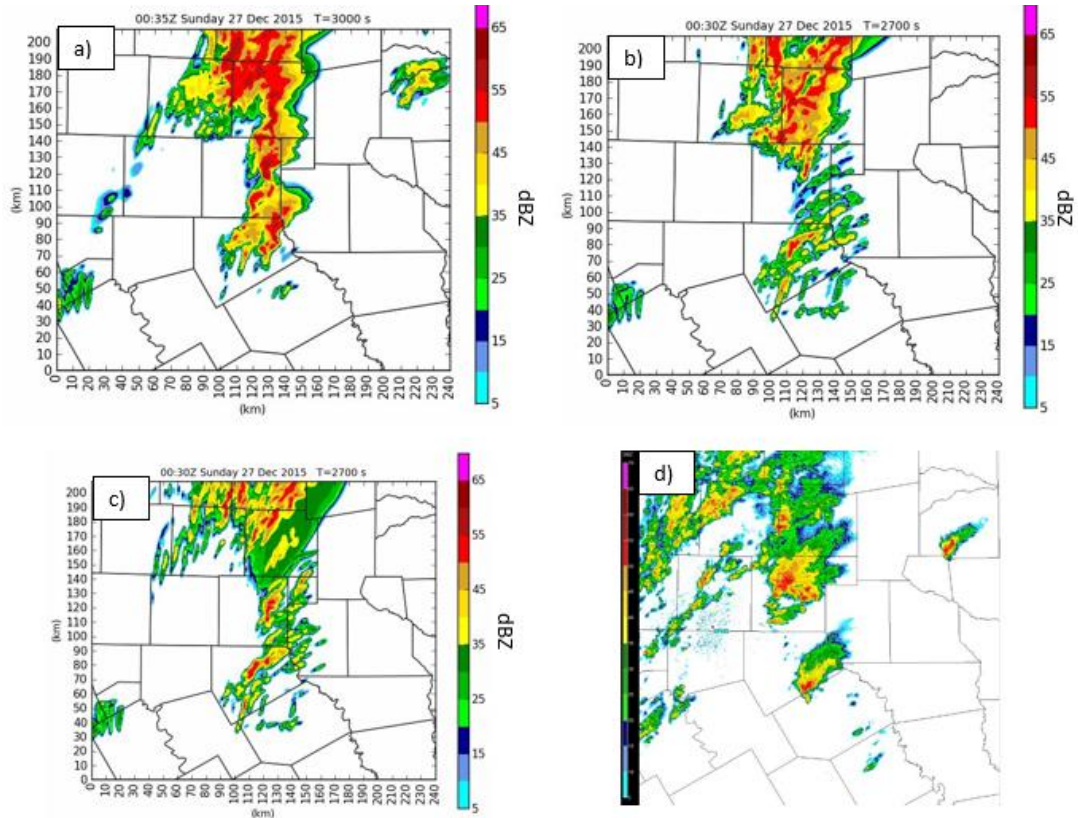
Figure 3.10: Comparison of 1 km AGL reflectivity field 45 minutes into the free forecast at 0030 UTC on 27 December 2016 for experiments a) CTL, b) NO88D, and c) NORADAR, and d) KFWS observed 0.5°.

The NORADAR experiment has not had as much time for the storms to mature which would explain why the reflectivity overestimate is not as extreme in that experiment. Focusing on the tornadic Rowlett storm in east central Dallas County at this time, the CTL experiment matches better with the observed appearance of the storm. Both the NORADAR and NO88D experiments (Figs. 3.10b,c) have a disorganized collection of convective cells in the area of eastern Dallas County where

there is a clearly defined supercell in the CTL experiment and the observed reflectivity field. This is likely the result of the model being able to develop the supercell into a more organized state at an earlier time when it is provided with information about the storm at the initial time. The supercell is on the periphery of the CASA network at this time, with only the southernmost available CASA radar (Midlothian, XMDL) having the storm within its range. The storm is completely outside of the TDWR network at the final analysis time. A comparison of closest WSR-88D radar (KFWS) observed composite reflectivity (Fig. 3.11a) at 2345 UTC with the observed composite reflectivity from XMDL (Fig 3.11b), the closest CASA radar to the storm at this time, reveals the lack of reflectivity information available when WSR-88D radar data is not included. Substantial attenuation effects (from a storm producing heavy precipitation over the radar site) on the X-band signal seem to result in an erroneously low reflectivity representation of the Rowlett storm from the XMDL radar; further analysis is needed to confirm that is the cause of this effect. Examining the XMDL composite reflectivity at 2335 UTC (Fig. 3.12), there was a stronger echo associated with the Rowlett storm for this first analysis time but any information on the reflectivity field for the storm seems to have been lost in the second analysis cycle. Without this information in the NO88D and NORADAR experiments, the model is forced to generate the Rowlett storm on its own which delays the rotational development process. In this case, the expansive range of the 88D radar network is important as it is able to observe the Rowlett storm echo while the auxiliary radar networks (CASA and TDWR) do not provide the necessary coverage in this part of the domain. Experiments without

the 88D radar data do not capture the initial state of the storm and the result is a loss of accuracy in the subsequent prediction of the Rowlett tornadic supercell.
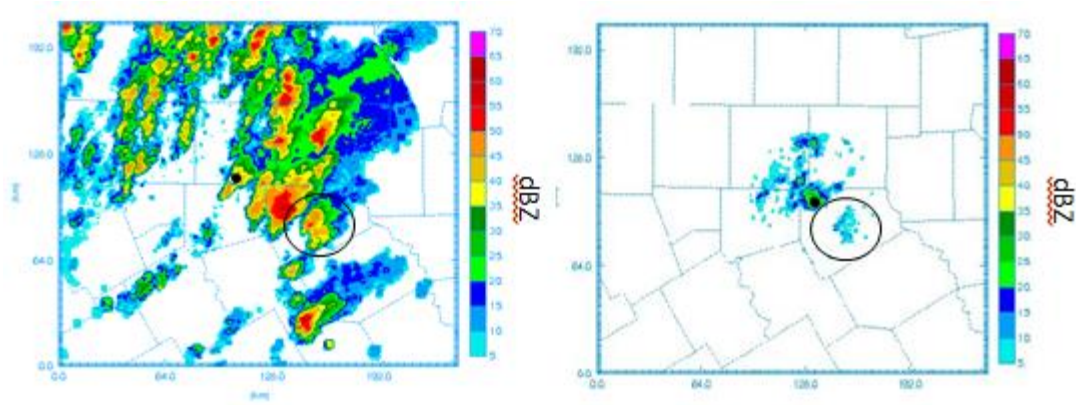
Figure 3.11: observed composite reflectivity at 2345 UTC from a) KFWS and b) XMDL. The location of the Rowlett storm is circled in black with the location of each radar identified with a black dot.

The nine experiments other than NO88D and NORADAR show little difference among them in their representation of the reflectivity field. The NOCASA experiment does look slightly different than the CTL experiment in its depiction of the Rowlett storm. The hook echo in the reflectivity field appears to be more pronounced in the NOCASA experiment (Fig. 3.13a) at 0025 UTC compared to the CTL experiment (Fig 3.13b) although the difference is not overwhelming. This subtle difference would suggest a better organized, faster-rotating mesocyclone in the case where CASA radars are denied, and this ends up being shown clearly in the plots of updraft helicity presented later on. The possible reasons for this will be addressed in later sections.
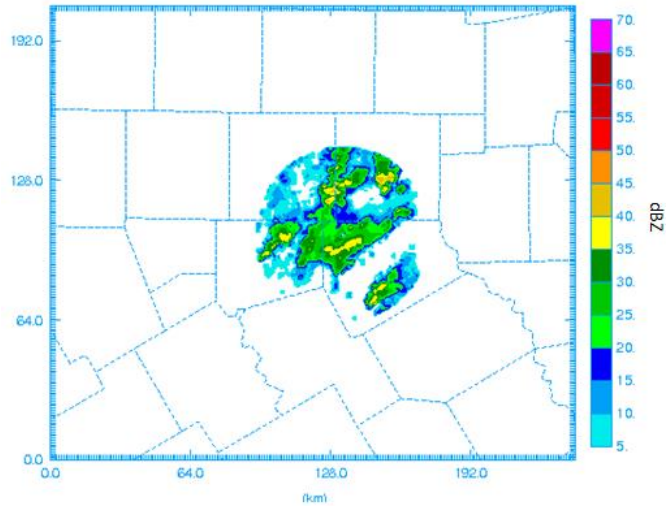
Figure 3.12: XMDL observed composite reflectivity at first analysis time (2335 UTC).
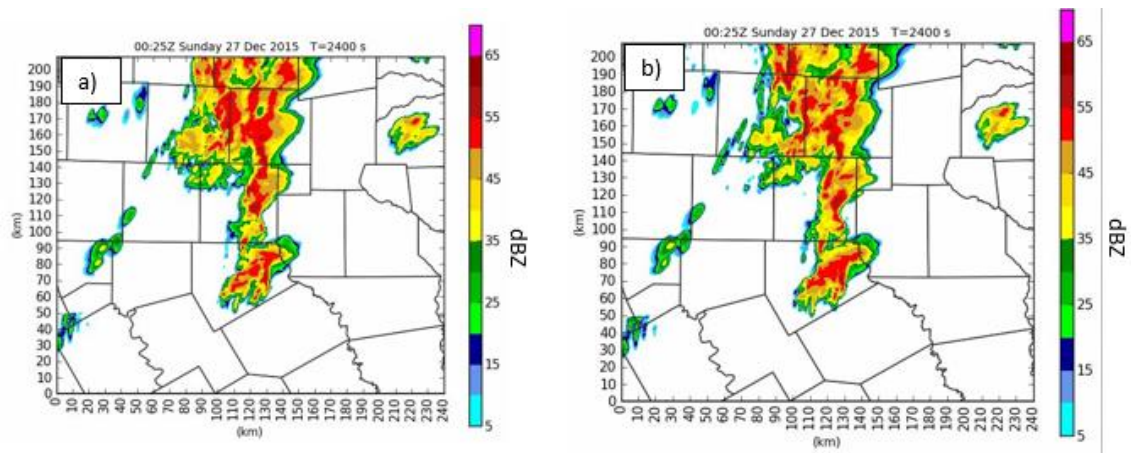
Figure 3.13: Comparison of 1km AGL reflectivity at 0025 UTC on 27 December 2016 for experiments a) CTL and b) NOCASA.
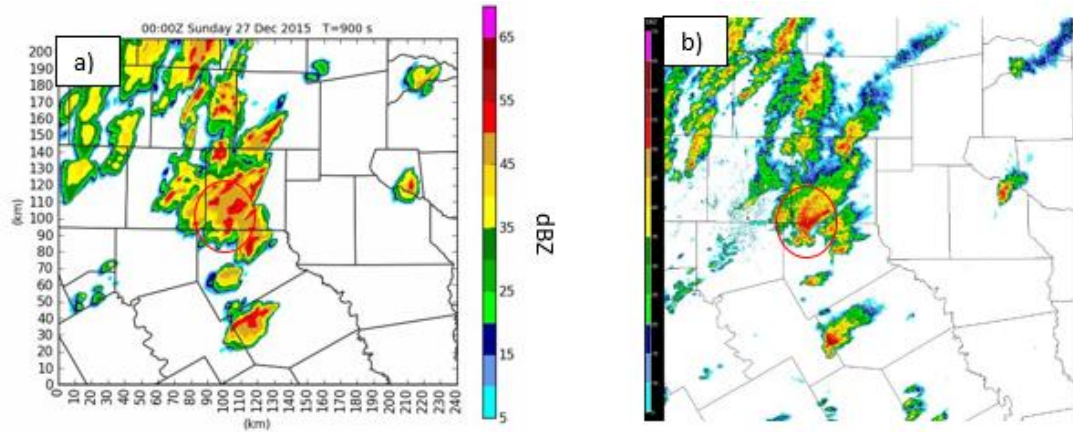
Figure 3.14: Comparison of 1 km AGL reflectivity at 0000 UTC on 27 December 2015 for a) CTL experiment and b) observed from KFWS. The Ovilla storm is outlined in red.

The Ovilla tornado was ongoing at the beginning of the forecast period for these experiments. Interestingly, none of the experiments, including the CTL experiment (Fig. 3.14a) are able to develop the hook echo feature seen in the observed reflectivity field (Fig. 3.14b) associated with the Ovilla tornado at 0000 UTC. The likely cause of this can be seen in the CTL reflectivity field in Figure 3.14a which shows more interference from the merging storm to the southeast than in the observed reflectivity. This interference leads to a lack of inflow which reduces the circulation in the model compared to what was observed. Another factor in these model runs not capturing the rotation with the initial tornadic supercell may be that the Ovilla tornado occurs within 15 minutes of the initialization time for the free forecast. This may not be enough time for the model to adequately develop and capture the intensity of the storm as it adjusts to the new information provided in the assimilation process.

3.4.2 FSS reflectivity verification

For a quantitative comparison of the reflectivity field between experiments, fractions skill score (FSS) values are computed. FSS is a probabilistic-based verification metric which compares fractional coverage of observed and forecast events within neighborhoods of grid points (Ebert 2008). The equation used to compute the FSS value is

$$FSS = 1 - \frac{FBS}{\frac{1}{N}\left[\sum_N \langle P_y \rangle_s^2 + \sum_N \langle P_x \rangle_s^2\right]} \quad (3.1)$$

where FBS is the fractions Brier score which is calculated via equation 3.2,

$$FBS = \frac{1}{N}\sum_N (\langle P_y \rangle_s - \langle P_x \rangle_s)^2 \quad (3.2)$$

where, $\langle P_y \rangle_s$ is the fraction of grid points with forecasted values greater than a threshold value within the specified neighborhood, $\langle P_x \rangle_s$ is the fraction of grid points with observed values greater than a threshold value within the specified neighborhood, and N is the number of neighborhood windows in the domain.

This metric is more appropriate than the traditional grid-based verification measures for convective scale forecasts because predictability decreases at higher resolutions. Accordingly, the FSS computation gives a high tolerance for slight spatial errors in the fields of interest, such as precipitation or reflectivity, which would be double-penalized by traditional verification measures (Ebert 2008). FSS for 1 km AGL reflectivity is

computed over a range of neighborhood scale sizes and reflectivity threshold values. Figure 3.15 shows how the average FSS for the forecast period varies with increasing neighborhood size for each experiment. The skill score does increase as the number of grid points involved in the computation in each neighborhood increases, but the value of the enhanced model resolution is lost as the neighborhood size is increased. The goal is to find a neighborhood length scale for which the model skill is useful yet the field is not overly smoothed. The FSS value for all experiments decreases as the reflectivity threshold value is increased from 20 dBZ (Fig. 3.15a) to 30 dBZ (Fig 3.15b) and then to 40 dBZ (3.15c). This indicates the lower threshold values are more predictable in the model simulations. Roberts and Lean (2008) define $FSS_{uniform}$, represented by the dotted line in Figure 3.15, as the score halfway between that of a random forecast and a perfect forecast which they found to be a suitable skill threshold. The scale at which this $FSS_{uniform}$ value is first reached at the 20 dBZ threshold is shown for each experiment in Figure 3.15. For the majority of the experiments, the $FSS_{uniform}$ scale is 6 grid points (2.4 km). The two experiments which were shown to be qualitatively less accurate in the previous section require a larger neighborhood size to show useful forecast skill. For the NO88D experiment, the $FSS_{uniform}$ scale is 12 grid points (4.8 km) while for the NORADAR experiment it is 124 grid points (49.6 km). The NORADAR experiment average FSS score stays below all the other experiments for all scales and for all reflectivity threshold values. The NO88D experiment average FSS score is lower than the other experiments for the most predictable threshold (20 dBZ). The CASA and TDWR radars provide some reflectivity information for the final analysis which results in better reflectivity skill in the NO88D experiment compared to the NORADAR

50

experiment which takes 15 minutes to initiate precipitation without any radar data available. The 17 grid point neighborhood is the smallest length scale at which the FSS metric is able to show skill values above $FSS_{uniform}$ for most of the experiments and so this was seen as a good scale to look at variations of FSS values from each experiment over the forecast period. This time series (Figure 3.16) shows an FSS value of zero for the initial 15-minute period in the NORADAR experiment where no reflectivity is present and a corresponding rise in the FSS value as the model starts to initiate the convective precipitation. A similar pattern is seen in the NO88D time series for the 20 dBZ threshold with the missing storms outside of the CASA/TDWR networks at the initial time likely contributing to decreased FSS values compared to the other experiments. The other experiments are generally closely clustered in the FSS plots with the NO88D and NORADAR experiments converging to the other experiments further into the forecast period when the missing storms are initiated within the model for those experiments. The NO88D experiment does show better skill than the other experiments for the larger neighborhoods at the higher thresholds (20 and 30 dBZ). This is likely attributable to the overestimate of higher values of reflectivity in these experiments. The NO88D experiment takes longer to spin up some of the heavier convective elements and so the overestimate is not as large in this experiment. Overall predictability of the reflectivity field is good for most of the experiments at the 20 dBZ threshold with FSS values staying above the $FSS_{uniform}$ threshold for the first 40 minutes of the simulation.
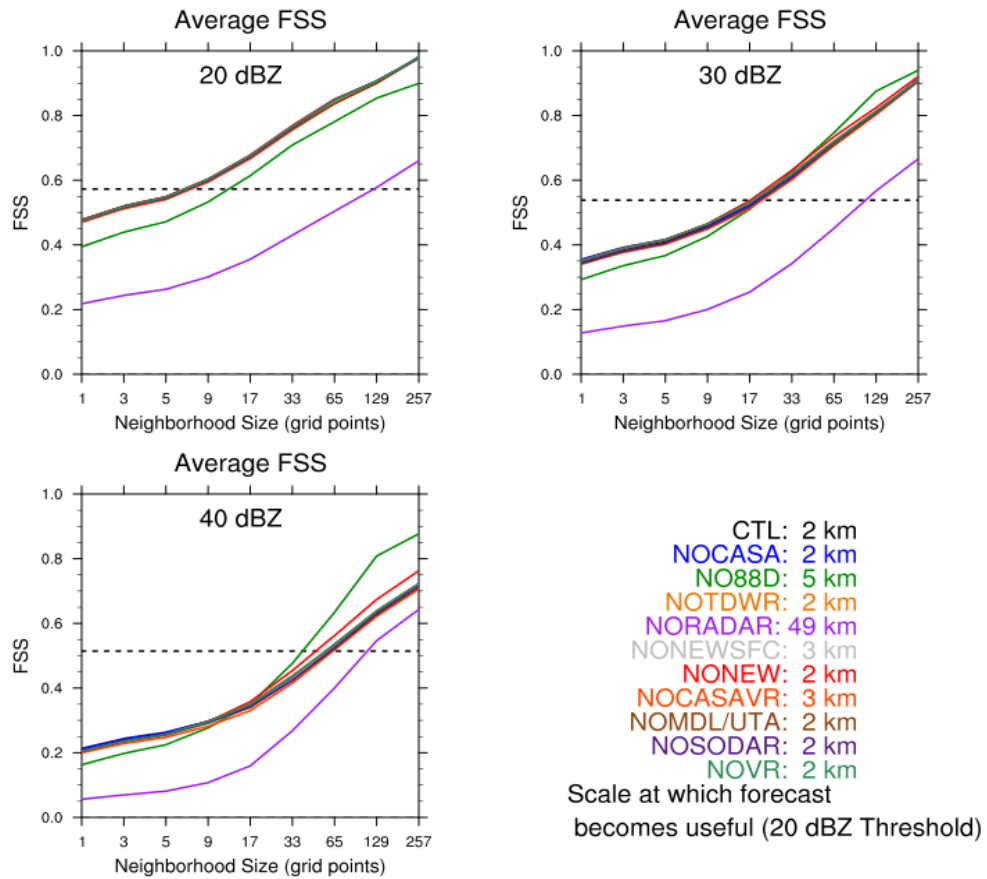
Figure 3.15: Average 1 km AGL reflectivity FSS for the 11 experiments over 9 different neighborhood sizes for a) 20 dBZ threshold, b) 30 dBZ threshold, and c) 40 dBZ threshold. The bottom right panel shows the FSS$_{uniform}$ scale in grid points for the 20 dBZ threshold for each experiment, while the dashed line plotted is the FSS$_{uniform}$ value for each threshold.
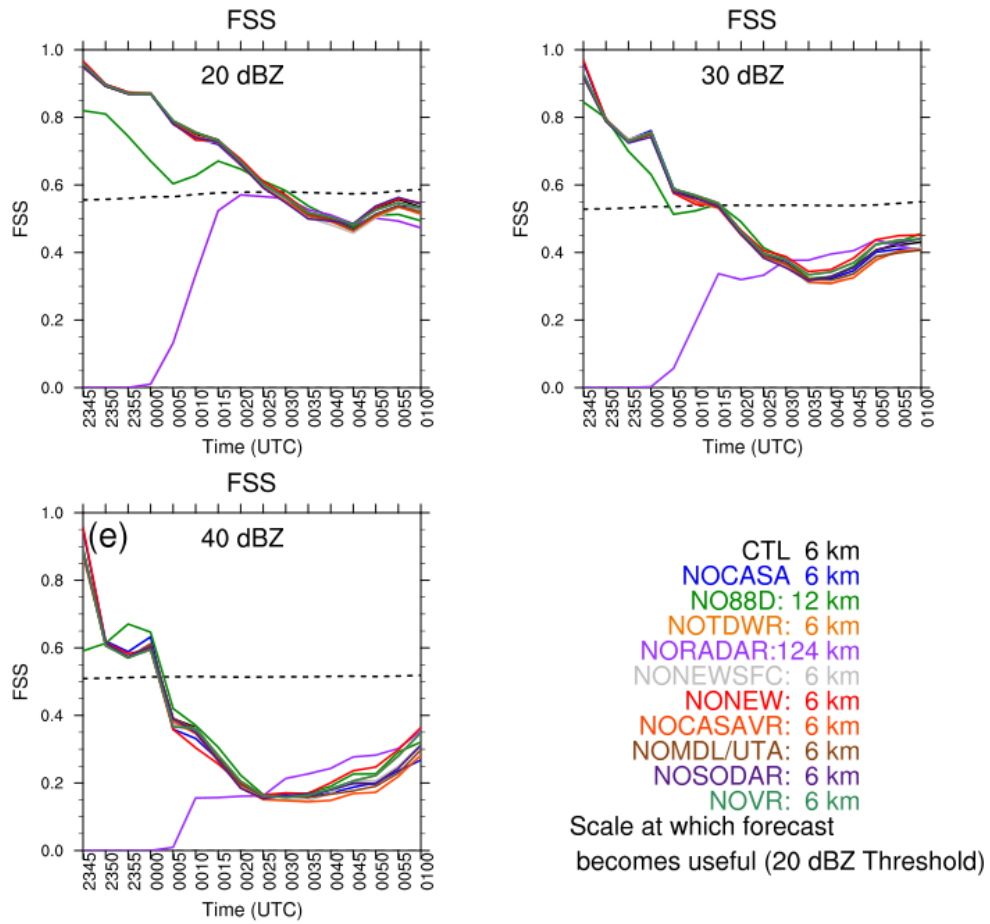
Figure 3.16: Time series of 1 km AGL reflectivity FSS value for all 11 experiments over the forecast period using a neighborhood size of 17 grid points for a) 20 dBZ threshold, b) 30 dBZ threshold, and c) 40 dBZ threshold. Values in the bottom right panel and dashed lines are the same as in Fig. 3.12

3.4.3 Rotation Track Comparison

Several of the experimental forecasts end up with strong, trackable 0-1 km updraft helicity (UH) centers. Updraft helicity is an integrated quantity combining updraft speeds with vertical vorticity (Kain et al. 2008). Stratman and Brewster (2015) have shown that comparison of model-produced UH fields with observed tornado locations is an effective model forecast verification tool in tornadic cases. Figures 3.17 and 3.18 show swaths of 0-1 km UH for each experiment plotted every 5 minutes along with the

observed tornado track (orange line) based off of the NWS damage survey. For the majority of these experiments, the rotation center moves to the northeast parallel to the observed tornado track with a slight turn to the northwest before dissipating. Overall, the tracks are fairly accurate, they are similar in length and location with about 10 km difference in average location between the westernmost and easternmost tracks. Also included for comparison is the radar observed rotation track product from the National Severe Storms Laboratory (NSSL) (Fig. 3.17e). The experiments that do not end up with a coherent UH track are the NO88D and NORADAR experiments. Each of the other experiments have at least 10 minutes of elevated 0-1 km UH values (> 200 m^2/s^2). As mentioned in the reflectivity verification section, the 88D radar network is the only one of the three networks that is able to provide reliable reflectivity observations of the Rowlett storm during the final analysis time of 2345 UTC. The XMDL CASA radar has a weak velocity signal (Fig 3.19b) at this time in the area of the Rowlett storm, while the KFWS 88D radar has a much stronger velocity signal (Fig. 3.19a) with some evidence of a rotating updraft developing in the Rowlett cell. The 88D radar also clearly observes the rotation in the more mature Ovilla storm, which is not evident from the CASA radar data. Without the necessary radar reflectivity and velocity information in both the NORADAR and NO88D experiments, the storm is not present in the analysis at the initial forecast time. The lack of initial convective-scale representations of precipitation and velocity within the Rowlett storm forces the model to initiate the supercell storm and generate a rotating updraft on its own. This does not allow time for development of a mature supercell with a substantial low-level mesocyclone within the one hour and fifteen minute period of the free forecast. Later observations from the

54

XMDL radar show higher reflectivity and stronger velocities associated with the Rowlett storm (Fig 3.20). Further experiments starting around 10 to 15 minutes later using these less attenuated XMDL observations may provide different results, especially with respect to the impact of the CASA radar data.

For the other nine experiments which forecast a coherent, trackable UH center associated with the Rowlett supercell, the tracks show in Figure 3.16 and 3.17 are mostly 5 to 10 km east of the observed tornado track. This spatial difference between observed and simulated rotation track is also evident in the plot of the track errors seen in Figure 3.19. An object-based technique from Stratman and Brewster (2015) was used to identify maximum UH centers for each experiment every 5 minutes. The algorithm looks for grid points with UH values greater than 80 m^2/s^2 and 7 of 8 surrounding grid points greater than 40 m^2/s^2 with a minimum distance between centers set to 10 grid points. These values were found to be the most suitable for identifying the main rotation centers leaving out any ancillary sub-vortices. When comparing the UH center for each experiment to the nearest observed tornado point at any time the difference has a positive x component (eastward shifted track) (Fig. 3.21b). The difference in timing of the rotation track can be seen by the same time (ST) track error plot (comparing forecast and observed rotation at the same verification time) in Figure 3.21a where most of the points are in the northeast quadrant indicating a faster progression of the rotational center in the simulations. This faster progression was also seen in the real-time CAPS forecast for this case and could be due to errors in the flow field (steering flow) introduced by using a 6 hour NAM forecast for the initial condition

Figure 3.17: Forecasted 0-1 km maximum updraft helicity every 5 minutes for a) CTL, b) NOCASA, c) NOCASAVR, d) NOMDL_NOUTA. Radar-observed NSSL rotation track is shown in e). NWS estimated damage path is overlaid as a black line in a)-d) and an orange line in e).
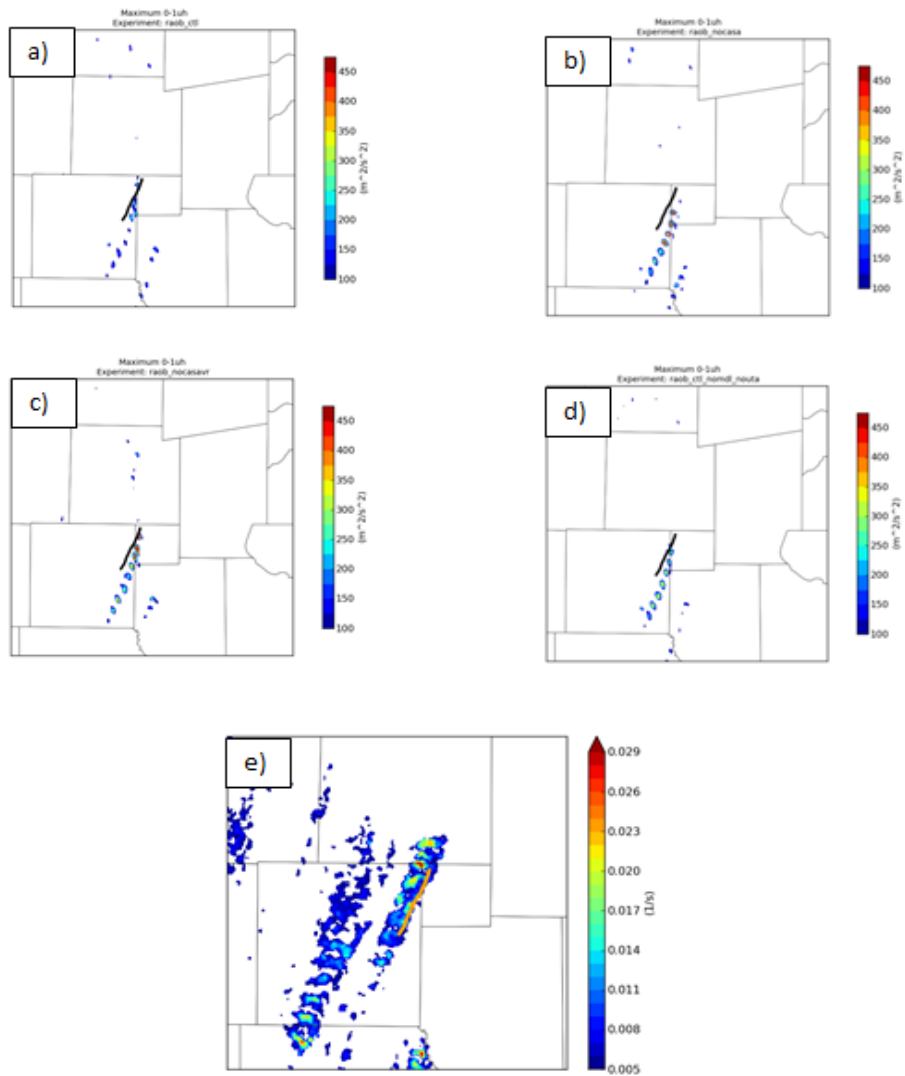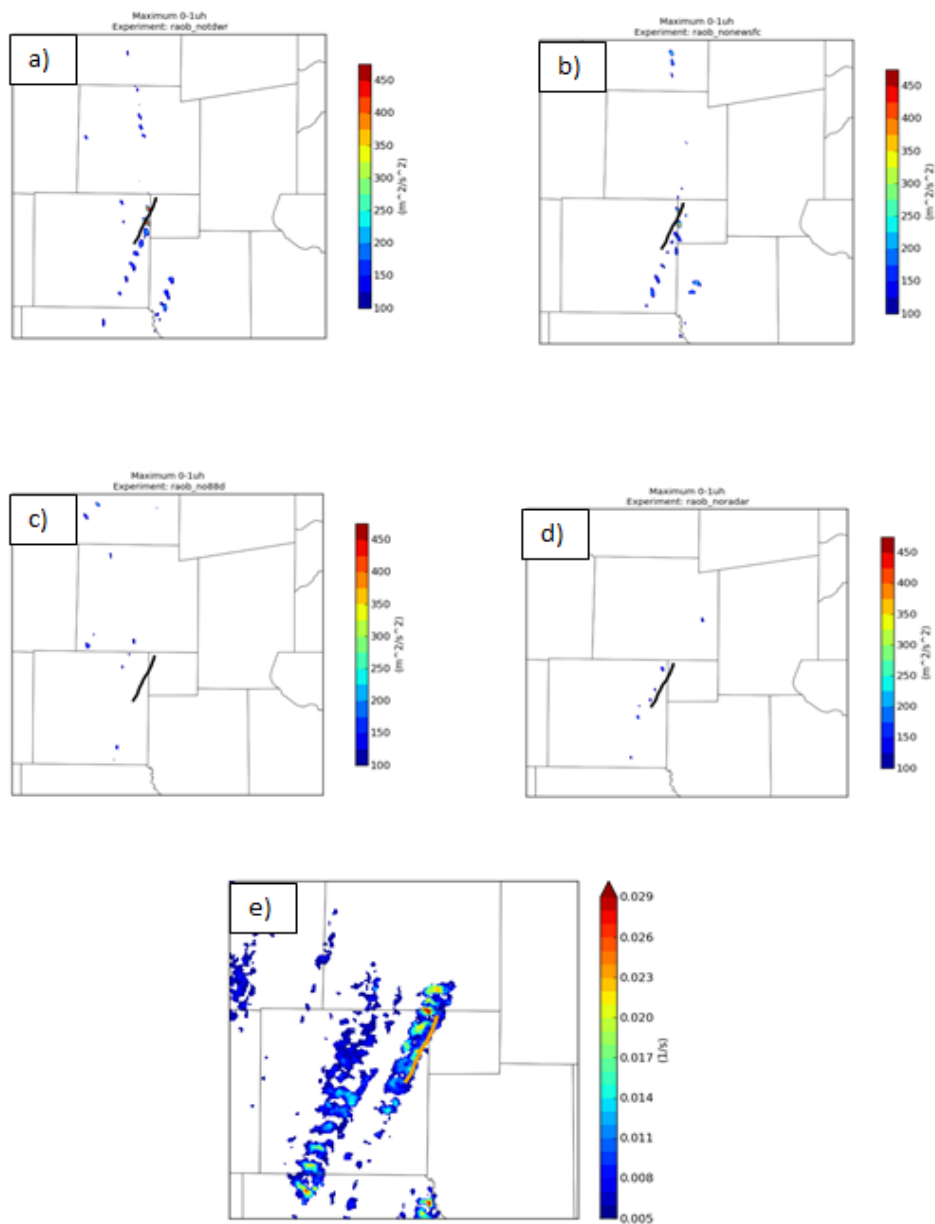
Figure 3.18: Forecasted 0-1 km maximum updraft helicity every 5 minutes for a) NOTDWR, b) NONEWSFC, c) NO88D, and d) NORADAR. Radar-observed NSSL rotation track is shown in e). NWS estimated damage path is overlaid as a black line in a)-d) and an orange line in e).

or due to accelerated propagation by excessive rainfall and/or cold pool strength in the Lin scheme.

Even with the speed error, most of the forecasts place a strong UH center within 10 km of the observed tornado which is remarkably accurate for a 45 min to 75 min forecast from an assimilation and forecasting system that can be run in real-time today.
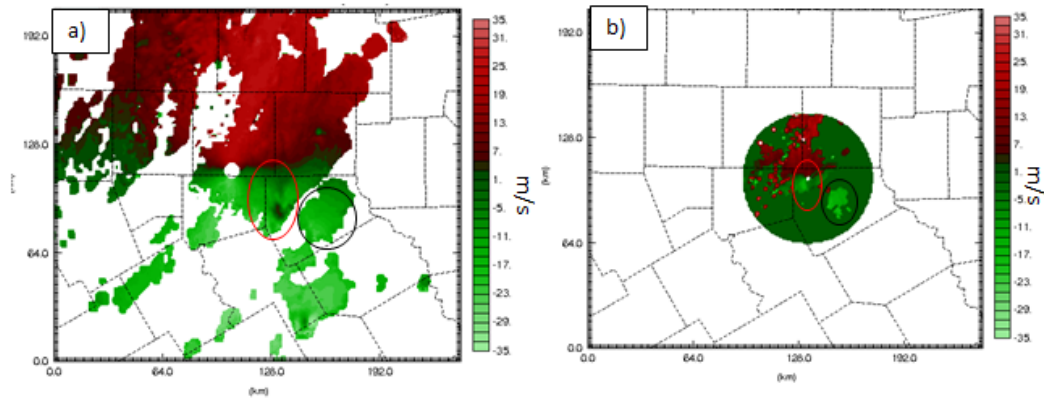
Figure 3.19: observed 1 km AGL radial velocity at 2345 UTC for a) KFWS and b) XMDL

The main differences in the plotted UH swaths come in the intensity values across experiments. A time series of the maximum 0-1 UH values for each experiment over the final 45 minutes of the forecast can be seen in Figure 3.22. Interestingly, the NOCASA experiment has the highest 0-1 UH value over the time period with a maximum value of nearly 1800 m^2/s^2 at 55 minutes into the free forecast. This experiment also shows the longest duration of sustained strong UH values greater than 400 m^2/s^2. On the other hand, CTL has a maximum UH value that is one of the lower ones of all the experiments. The CTL 0-1 UH never gets above 250 m^2/s^2 and the structure of the UH field (Fig. 3.16a) is less organized and more transient than the NOCASA field (Fig. 3.16b). Another experiment with relatively high maximum UH values is the NOTDWR

experiment with UH values up to 800 m^2/s^2. This indicates that the inclusion of the CASA radar data along with the TDWR data results in a simulated supercell with a combination of less low-level rotation and weaker updraft speeds than when one of these new radar networks is denied. As we don't have the observed 0-1 UH field associated with the EF4 tornado to compare these modeled values to, it is unclear which experiment has the more accurate rotational intensity estimate. The extra noise introduced in the wind field from the assimilated CASA radars could be a possible explanation for the differences in forecasted UH field initialized from these analyses or very early forecasts, but how this noise actually manifests itself in the analyzed and forecast wind field is not evident at this time. This difference between CTL and NOCASA led to experiments NOCASAVR and NOMDL_NOUTA being carried out to further examine the effects of the CASA radar data. NOCASAVR retains the CASA reflectivity within the assimilation process while denying the radial velocity from these radars. The 0-1 UH swath for this experiment (Fig. 3.16c) is much closer to the NOCASA run than the CTL run in terms of intensity of UH values along the track. This result suggests the CASA radial velocity data is more responsible for the lack of UH intensity and coherency within the CTL experiment than the CASA reflectivity data. Assimilated radial velocity directly alters the dynamic state which the UH is computed from. The CASA reflectivity data is likely to have reduced, indirect effects on the model dynamical fields via its inclusion in the complex cloud analysis. The cloud analysis mosaics the reflectivity from all radars using a maximum value algorithm, thus any attenuated X-band reflectivity is superceded by co-located S-band reflectivity from the 88D radars.

59
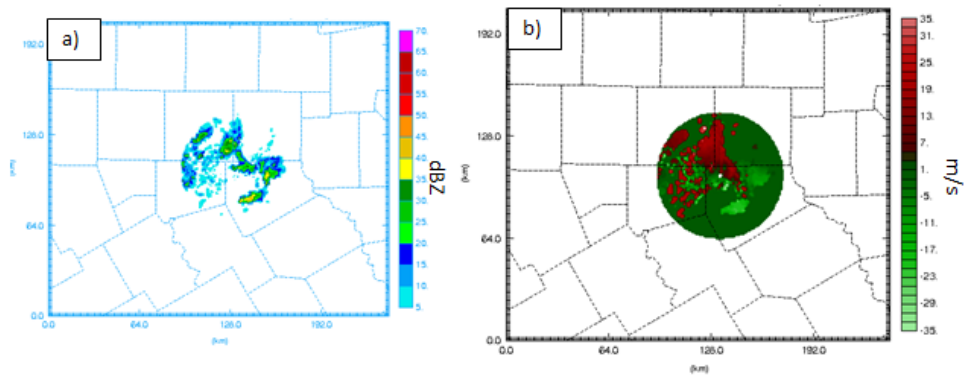
Figure 3.20: observed a) composite reflectivity and b) radial velocity on the 0.79° tilt at 0005 UTC from the XMDL CASA radar.
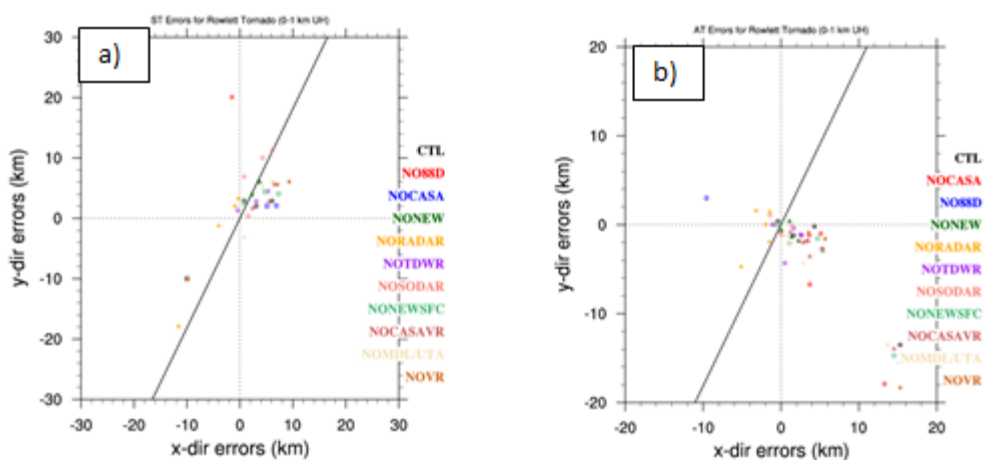
Figure 3.21: Difference between maximum UH center and closest observed tornado point a) at the same time and b) at any time for each five minute forecast from 0035 UTC to 0100 UTC.
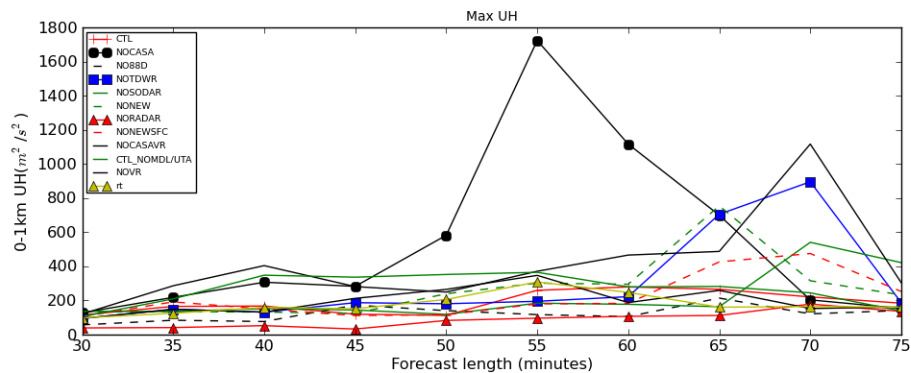
Figure 3.22: Maximum 0-1 km UH for each experiment plotted every 5 minutes from 0020 UTC to 0100 UTC.

The NOMDL_NOUTA experiment assimilates three of the five available CASA radars with the two closest to the Rowlett storm at the time of assimilation, XMDL and XUTA, being denied to examine the effect of proximity to storm location. Stronger, longer -lived 0-1 UH values are evident in this experiment (Fig. 3.16d) compared to the CTL run, although the maximum UH values are still below that of the NOCASA run. Thus, the difference in UH swaths between CTL and NOCASA is likely largely caused by effects introduced by the radial velocity data of the two closest radars. The 88D radar network is essential to an accurate model forecast of the rotating supercell moving close to the track of the observed tornado in this case. The combination of assimilating CASA and TDWR radars results in lowered maximum UH values compared to when one of the two networks is denied. The lack of positive impact from the CASA radars in this case is likely due to the storm being largely outside of the range of the network during the assimilation period. Stratman and Brewster (2015) came to a similar conclusion that the 88D radar (KTLX in that case) has more impact than the CASA radars for a storm that is not initially within the CASA network. The case studied here

is also more convectively active than previous CASA data impact studies and the effect of the CASA radars may not be as clear in these cases (Stratman and Brewster 2015).

3.4.4 Rainfall Comparison

An important aspect of the DFW urban testbed is its ability to evaluate the effect of the additional observations on rainfall and flash flood prediction. Towards this end, QPF values from each experimental model run are compared to the MRMS observed one hour gauge-adjusted Quantitative Precipitation Estimate (QPE) data over the forecast interval from 0000 UTC to 0100 UTC on 27 December 2015 over the 400 m WRF forecast domain. There is a clear overestimate of precipitation values from most of the model runs (Figure 3.23) compared to the observed QPE field (Figure 3.23a). This seems to be correlated well with the reflectivity fields shown earlier which overestimated the reflectivity compared to the KFWS observed reflectivity within many of the convective storms, especially in Collin County. To put the difference in perspective, the CTL run (Fig. 3.23b) has a maximum one hour accumulation value of 67.1 mm while the observed maximum accumulation over the same hour at any one point within the domain was 33.1 mm, less than half of the forecasted maximum. The overestimate is more exaggerated for the real-time CAPS forecast (not shown) from the same initial time with a maximum value of 154 mm. The difference between the real-time run and the experiments in this work is likely attributable to the cloud analysis being improved in the interim to remove a step that reduced the saturation of the airmass in areas of observed rain. Also, another differing factor is the WRF model being used here while the ARPS model is used for the real-time runs and there was problematic radiometer data assimilated in the real-time run which was not assimilated

here. The overestimate of precipitation in both cases can most likely be explained by inaccuracies introduced by the approximations used in the single-moment Lin ice microphysics scheme. The higher dew point values introduced by assimilation of many of the non-conventional surface stations, which will be explored in more detail in the next section, do not appear to be a major factor in the overestimate of precipitation in these experiments as the NONEWSFC experiment has QPF values that are similar to the CTL experiment. Looking at the shape and placement of the modeled QPF, the rainfall is displaced to the east from the observed precipitation field and is much more expansive in Collin County. The NO88D and NORADAR experiments (Figs 3.23c,d) do not feature as much widespread excessively heavy precipitation likely due to the spin-up required for the unobserved storm features which do not have as much time to develop intense precipitation regions during the forecast. Overall, the rainfall estimates from these experiments do not show the same level of predictability as the UH field for this particular case with this model/analysis setup.
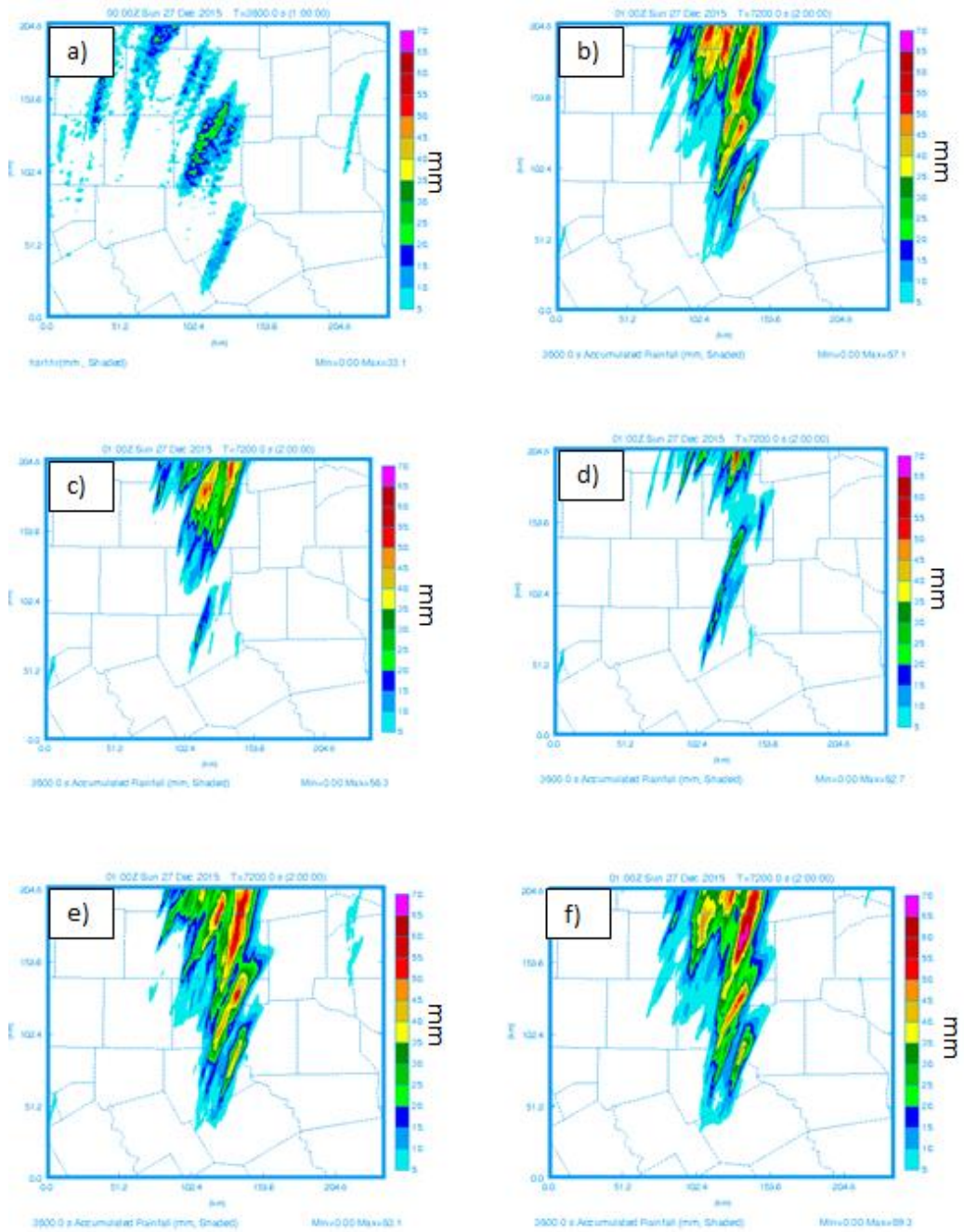
Figure 3.23: One hour accumulated rainfall in millimeters from 0000 UTC to 0100 UTC from a) MRMS radar observed/gauge adjusted QPE, b) CTL, c)NO88D, d)NORADAR, e)NOCASA, and f) NONEWSFC experiments.
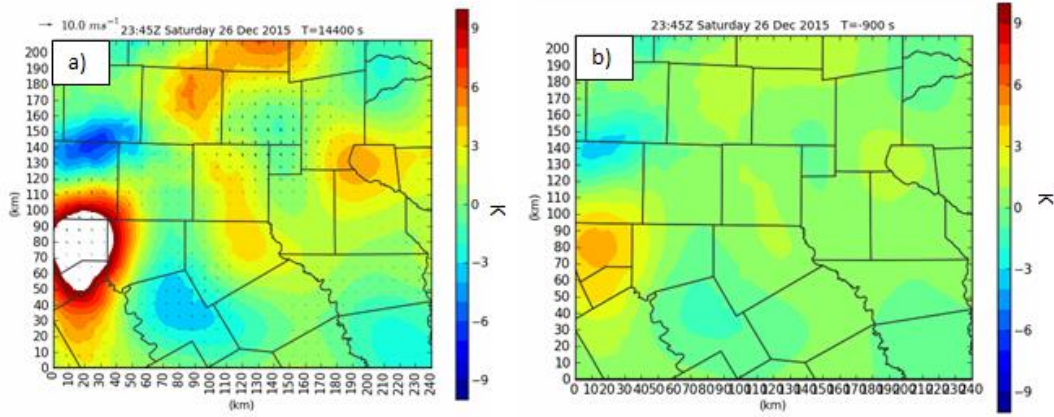
Figure 3.24: CTL-NONEWSFC a) equivalent potential temperature and b) dew point difference field in K at the final analysis time 2345 UTC 26 December 2015.
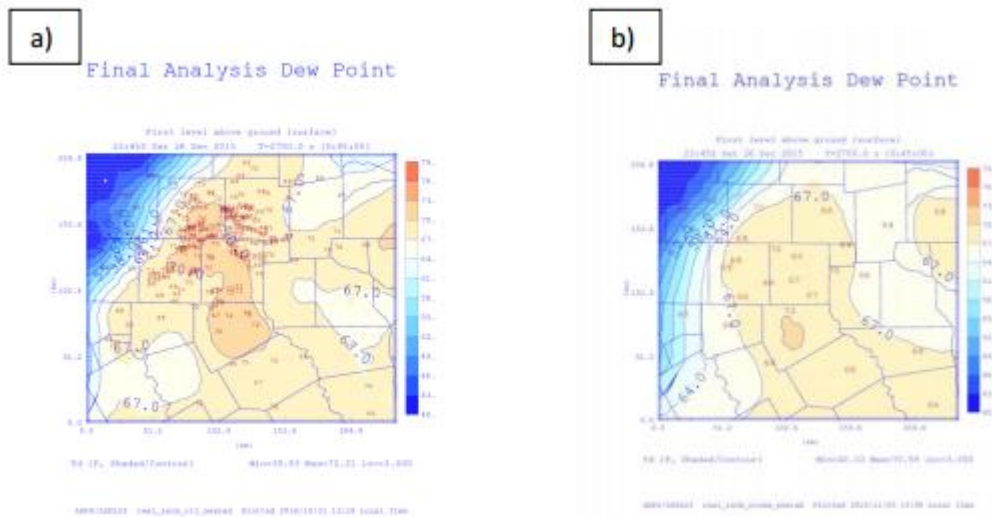
Figure 3.25: Dewpoint in °F at the lowest model level at the final analysis time (2345 UTC) for a) the CTL experiment and b) the NONEWSFC experiment. Non-conventional dew point observations overlaid in a) and ASOS/AWOS dew point observations overlaid in b).

3.4.5 Surface observation impact

Although the main focus of this work is radar data impacts, one of the experiments, NONEWSFC, was designed to look at the impact of non-federal surface data available in the DFW testbed. Carlaw (2014) found substantial positive impact on high resolution analyses from these observation types in an otherwise data sparse area in north central Texas southwest of Dallas. Using the WRF forecast model rather than the ARPS model for this tornadic case a similar surface observation impact result is evident. Looking at the surface equivalent potential temperature difference fields in Figure 3.24, the CTL experiment has equivalent potential temperature values that are 10 Kelvin warmer than those in the NONEWSFC run in Hood county. The dew point temperature in this area is on the order of 5 to 6 Kelvin warmer (Figure 3.25). There are several Weatherbug and CWOP stations in this vicinity and only one conventional AWOS station. The reason for the large moisture and instability differential in this area appears to be the cold front being held back more by the CTL experiment which includes more data to better define the temperature and moisture gradient. Further examination of the AWOS observation value in Granbury, TX in central Hood County indicates a substantial discrepancy. The dew point value assimilated from this AWOS station is 60°F while the surrounding CWOP and Weatherbug stations have dew points in the upper 60s (Figure 3.25). The low dew point value from the AWOS station is valid at 2355 UTC but is assimilated for the analysis at 2345Z. The boundary has likely moved over the station in this 10 minute time period and so the supplemental non-federal observations are able to correct for this temporal error associated with the strong moisture gradient. Thus, it is clear that with the presence of a strong gradient in the observed fields the additional observations are

66

key to more accurately defining the frontal structure in an area with a dearth of conventional observations. To the north of this large positive difference, there is a negative temperature difference in northern Parker County which indicates the CTL is picking up on the front being pushed farther to the south and east with the additional observations in this area. The orientation of the front is more southwest to northeast and there is a tighter moisture gradient in CTL than in NONEWSFC in this area as can be seen clearly in the dew point plots in Figure 3.25. There are no ASOS stations to verify against at this time within that portion of the domain so it is assumed that with more complete observational sampling of the frontal region, the CTL experiment is more accurately defining its placement and characteristics. The NONEWSFC experiment is relying more on the less accurate background forecast in these areas where there is a dearth of conventional surface data. The few conventional surface observations available in this vicinity are AWOS or mesonet stations, the prescribed quality of which prevent them from having as much weight in the analysis as the ASOS stations. These areas are similar to the Johnson County and Parker County area where Carlaw (2014) found substantial difference in experiments due to the non-conventional surface stations. The analysis differences in this case do not contribute as much to the actual forecast storm development in the more immediate DFW metropolitan area because that is well-displaced from these areas that are more sensitive to additional surface observations.

Ten ASOS stations were withheld from the experiments so that these could be used to verify the analyses and forecasts. A plot of root mean square difference over the forecast time period (Fig 3.26a) shows that the NONEWSFC experiment has higher

error in the latter half of the forecast than the CTL experiment. The plot of dew point bias (Fig 3.26b) shows that the NONEWSFC experiment is drier than the observations at the surface for the first part of the forecast followed by a period where the forecast is more moist than the observations. The CTL experiment has a moist bias throughout which would indicate the non-conventional surface observations are providing consistently higher dew point values than the conventional ASOS observations. This can be seen in Figure 3.25 where the analyzed dew point field has larger values in the immediate DFW metro area in the CTL experiment compared to the NONEWSFC experiment. Overall, there is a slight improvement in surface dew point forecast accuracy with the inclusion of the non-conventional surface information, although most of the ASOS stations used in the verification are not in the poorly-sensed areas where the non-conventional data is more likely to add value. Performing an analysis using the same method used in the assimilation cycles that initialize these experiment would likely provide a more useful verification dataset for the surface fields from which more definitive conclusions may be drawn about the added value of the non-conventional surface stations.
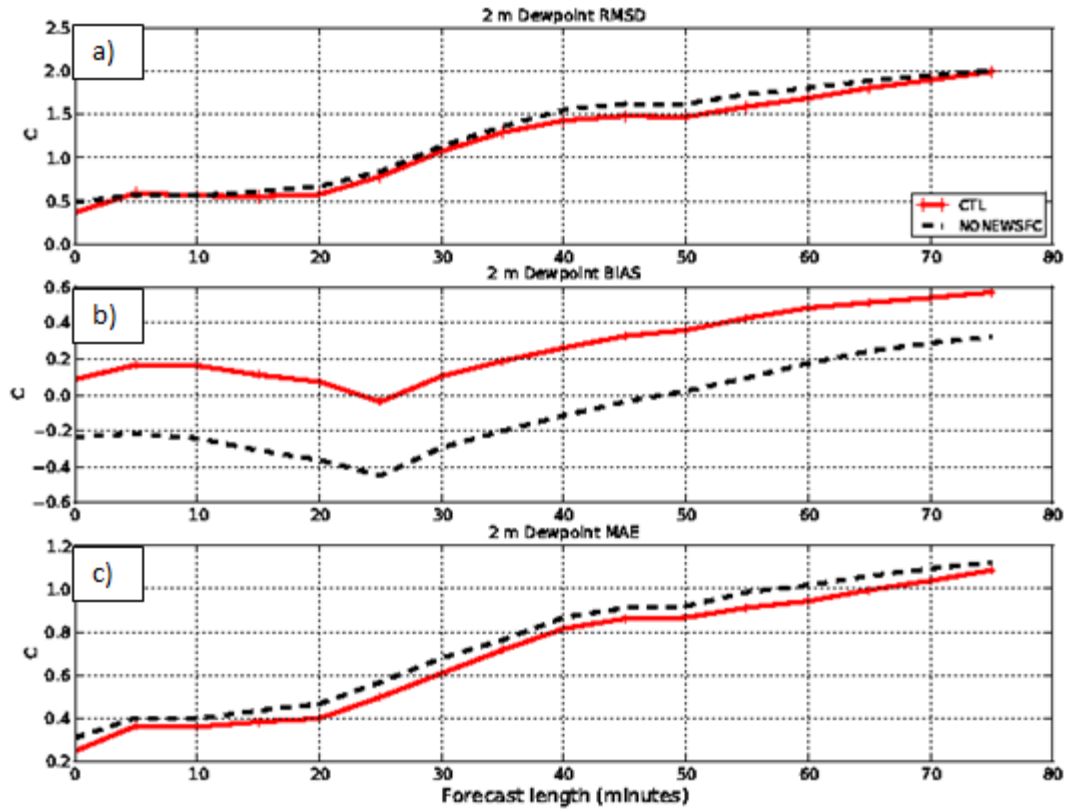
Figure 3.26: Plots of a) root mean square difference (RMSD), b) bias, and c) mean absolute error (MAE) every five minutes over the forecast period (2345 UTC-0100 UTC) for surface dew point based on 10 withheld ASOS station observations.

Chapter 4

4.1 Summary and conclusions

The work presented here has looked into the impact of several non-conventional data types in the DFW Urban Testbed within a high-resolution analysis and forecasting framework. The ARW-WRF was used to carry out the model simulations as this model has widespread operational use and these types of studies are most useful when their results can be easily applied to operational scenarios. One of the most notable, impactful events that has occurred in the DFW metro area over the time of the existence of the testbed was the 26 December 2015 tornado outbreak. Five of the eight CASA radars were installed and operational at this time and so this case was seen as a good way to evaluate the impact of those newly deployed radars. This is the first time this type of study has been done for the DFW CASA X-band radar network. Although the focus for this study is the impact of the CASA radar network, we also consider the impact of other non-standard observation types within the context of this DFW testbed setup (TDWR radars, non-conventional surface networks, SODARS).

Simulated low-level rotation tracks, reflectivity, rainfall, and surface thermodynamic fields were analyzed for the 11 experiments presented here. In most of the experiments very good predictions were made of the storm track, demonstrating the robustness of the efficient data assimilation system employed. There was not much differentiation in these fields among many of the experiments. The exception was for the experiment which denied the 88D radar data and the one that denied all radar data. The lack of accuracy in forecasted rotational and reflectivity fields for these two experiments appears to stem from the inability of the CASA and TDWR networks to properly

observe the storm on the edges of their range due to attenuation of the X-band signal by the core of the storm that happened to be right over the closest radar at the initial time. This issue with X-band radar networks was anticipated and described by Brewster et al. (2004). The 88D radar data was the only one that properly observed the storm of interest and so these experiments without the 88D radar data were not able to accurately initialize the supercell thunderstorm that became the Rowlett/Garland tornado. One experiment involving the non-conventional surface data showed that these extra observations were able to supplement the few conventional observations southwest of the Dallas metro area to more accurately resolve a sharp frontal moisture gradient. This was a similar result corresponding to a similar area where positive impact was found in Carlaw (2014), although here the storm of interest was less sensitive to the non-conventional observations in this area as it was displaced to the north and east in a region with a larger population of conventional observations.

Model simulations which did include the 88D radar data showed good predictability with strong, trackable 0-1 km UH centers mostly less than 10 km from the observed tornado track. There was a fast bias to the storms (5-10 minutes) likely an effect of the Lin ice microphysics scheme used here. The simulated reflectivity field showed similar structure to the observed reflectivity field for most of these experiments with useful skill for the 20 dBZ threshold up to 40 minutes into the forecast. There was a clear overestimate of reflectivity in the model forecasts likely associated with a wet bias in the microphysics scheme. This wet bias was also clearly seen in the accumulated QPF values compared to much smaller observed QPE values, although the wet bias has been reduced compared to when the CAPS real-time run was carried out for this event.

A lot of the difference in experiments is seen in the rotational intensity values associated with the storm of interest in each forecast. Assimilation of the CASA radar data along with data from the two other available radar networks results in decreased low-level rotational strength. When CASA radar data is only paired with WSR-88D radar data the rotational decrease is not as pronounced. Further experiments performed seem to suggest the decreased rotational magnitude is tied specifically to the radial velocity data assimilated from the closest CASA radars. The magnitude of observed 0-1 km UH values would be needed to determine if this decreased rotational intensity matches up with reality. Otherwise, the CASA radar data does not seem to be integral to the overall accuracy of the forecast of the tornadic supercell with sustained rotation in this case. The CASA network configuration relative to the storm of interest was not ideal with the storm remaining on the periphery of the existing network during the assimilation time. Thus, although this case was selected as the best candidate for testing the newly installed CASA network, there were very few suitable cases to choose from in the short time frame the data had been available and it would be worthwhile to examine a variety of other cases and other times from this case day before making definitive conclusions about the impact of the CASA X-band radar network in the DFW testbed. Two more CASA radars have been added to the network, giving a total of 7 of 8 planned now operational, and they should provide additional coverage in the winter and spring of 2017.

4.2 Future Work

These results serve as the starting point for assessment of the DFW X-band CASA radar network. Future studies can help expand upon the conclusions drawn here by

looking at impact over a wide variety of convective events. The main goal of future studies should be to identify a case in the DFW area, similar to the case in Oklahoma presented in Stratman and Brewster (2015), where there is a storm developing near the center of the CASA radar network which would provide a better framework for making definitive assessment of the radar data impact. The CASA radar network has been expanded to 7 (and soon to be 8) radars including a recent installation in Mesquite which could have provided a good view of this storm from a unique angle had it been installed at that time. An ideal case to truly test the CASA concept would be in an area where there are adaptively-scanning CASA radars and an 88D radar that is farther away than the one in the DFW network such that the only low-level radar data would be coming from the X-band radars. This second effect could also be achieved in the DFW testbed by only assimilating 88D information from the higher elevation angles. The 26 December 2015 case could be further evaluated by looking into the effect of shifting the assimilation time up by 10 to 15 minutes to see if the storm is better observed by the CASA network at this time and to see if that changes the subsequent impact on the forecast. Looking at some of those times, the real-time analyses at 0000 UTC seemed to have captured the circulation of the Ovilla storm which had a tornado on the ground at that time. So although it would have been too late to provide lead time on the Ovilla tornado it may have created a better depiction of the Rowlett storm well ahead of the Rowlett tornado.

In order to have the results be more completely operationally relevant, future experiments should also compare the use of the GSI hybrid EnKF data assimilation system rather than the simpler 3DVAR analysis scheme. Also, it would be worth

73

investigating the effect of using a double-moment microphysics scheme for this or other cases to see if the overestimate of precipitation can be improved to better match observed rainfall values. Also, verification of rotational intensity could be achieved via creation of an analysis at specified verification times which would provide more definitive information about the low-level UH values associated with this tornado.

Bibliography

Aksoy, A., David C. Dowell, and Chris Snyder, 2009: A multicase comparative assessment of the ensemble Kalman filter for assimilation of radar observations. Part I: Storm-Scale Analyses. *Mon. Wea. Rev.,* **137**, 1805–1824, doi: 10.1175/2008MWR2691.1.

Alapaty, K., N. L. Seaman, D. S. Niyogi, and A. F. Hanna, 2001: Assimilating surface data to improve the accuracy of atmospheric boundary layer simulations. J. Appl. Meteor., 40 (11), 2068–—2082.

Agusti-Panareda, A., A. Beljaars, C. Cardinali, I. Genkova, and C. Thorncroft, 2010: Impacts of assimilating AMMA soundings on ECMWF analyses and forecasts. *Wea. Forecasting*, **25 (4)**, 1142-1160.

Barnes, S. L., 1964: A technique for maximizing details in numerical weather map analysis. Journal of Applied Meteorology, 3 (4), 396–409.

Benjamin, S. G., B. D. Jamison, W. R. Moninger, S. R. Sahm, B. E. Schwartz, and T. W. Schlatter, 2010: Relative short-range forecast impact from aircraft, profiler, radiosonde, VAD, GPS-PW, METAR, and Mesonet observations via the RUC hourly assimilation cycle. *Mon. Wea. Rev*., **138 (4)**, 1319–1343, doi:10.1175/2009MWR3097.1, URL http://journals.ametsoc.org/doi/abs/10.1175/2009MWR3097.1.

Bi, L., J. A. Jung, M. C. Morgan, and J. F. Le Marshall, 2011: Assessment of assimilating ASCAT surface wind retrievals in the NCEP global data assimilation system. *Mon. Wea. Rev.*, **139 (11)**, 3405-3421.

Bloom, S., L. Takacs, A. Da Silva, and D. Ledvina, 1996: Data assimilation using incremental analysis updates. *Mon. Wea. Rev.,* **124 (6)**, 1256–1271.

Bouttier, F., and G. Kelly, 2001: Observing-system experiments in the ECMWF 4D-Var data assimilation system. *Quart. J. Roy. Meteor. Soc.*, **127 (574)**, 1469–1488.

Brewster, Keith, 2003: ADAS/ARPS data assimilation using incremental analysis updating. Accessed 12 October 2016. [Available online at http://www.caps.ou.edu/ARPS/ARPS5DOC/ADASNudging.pdf]

Brewster, K., M. Hu, M. Xue, and J. Gao, 2005: Efficient assimilation of radar data at high resolution for short-range numerical weather prediction. *World Weather Research Program Symposium on Nowcasting and Very Short-Range Forecasting*, WSN05, Tolouse, France, WMO, Symposium CD, Paper, Vol. 3.

Brewster, K., K. Thomas, J. Brotzge, Y. Wang, D. Weber, and M. Xue, 2007: High

resolution data assimilation of CASA X-band radar data for thunderstorm forecasting. *22nd Conf. Wea. Anal. Forecasting/18th Conf. Num. Wea. Pred*.

Brewster, Keith, Brotzge, J., Thomas, K. W., Carr F. H., 2014: A real-time high-resolution analysis and short-term forecast system for severe weather in the Dallas/Fort Worth testbed. *27th Conference on Severe Local Storms*, Madison, WI, Amer. Meteor Soc.

Brewster, Keith, F. Carr, K. Thomas, D. Stratman, 2015: Utilizing heterogenous radar systems in a real-time high resolution analysis and short-term forecast system in the Dallas/Fort Worth testbed. *37th Conference on Radar Meteorology*, Norman, OK.

Cardinali, C., 2009: Monitoring the observation impact on the short-range forecast. *Quart. J. Roy. Meteor. Soc.*, **135 (638)**, 239-250.

Carlaw, Lee, 2014: Evaluating the impact of assimilating surface observations on high-resolution analyses and forecasts. M.S. Thesis, School of Meteorology, University of Oklahoma, 98 pp.

Carlaw, L. B., J. A. Brotzge, and F. H. Carr, 2015: Investigating the impacts of assimilating surface observations on high-resolution forecasts of the 15 May 2013 tornado event. *Electronic J. Severe Storms Meteor.,* **10 (2)**, 1-34.

Cha, Dong-Hyun and Yuqing Wang, 2013: A dynamical initialization scheme for real-time forecasts of tropical cyclones using the WRF model. *Mon. Wea. Rev.,* **141**,964-986, doi: 10.1175/MWR-D-12-00077.1.

Chou, M.-D., and M. J. Suarez, 1994: An efficient thermal infrared radiation parameterization for use in general circulation models. NASA Tech. Memo, 104606 (3), 85.

Clark, Adam, John S. Kain, Patrick T. Marsh, James Correia Jr., Ming Xue, and Fanyou Kong, 2012: Forecasting tornado pathlengths using a three-dimensional object identification algorithm applied to convection-allowing forecasts. *Wea. Forecasting,* **27**, 1090-1113, doi: 10.1175/WAF-D-11-00147.1.

CWOP, 2014: Hourly number of weather stations on APRS-IS. URL http://www.wxqa.com/checkservers2.html.

Dabberdt, W. F., and Coauthors, 2005: Multifunctional mesoscale observing networks. *Bull. Amer. Meteor. Soc.*, **86 (7)**, 961–982.

Dawson, I., T. Daniel, and M. Xue, 2006: Numerical forecasts of the 15-16 June 2002

southern plains mesoscale convective system: Impact of mesoscale data and cloud analysis. *Mon. Wea. Rev.*, **134 (6)**, 1607-1629.

Ebert, E.E., 2008. Fuzzy Verification of high-resolution gridded forecasts: a review and proposed framework. Meteorol. Appl. 15, 51-64.

Eilts, M. D., and S. D. Smith, 1990: Efficient dealiasing of doppler velocities using local environment constraints. *J. Atmos. Oceanic Technol.*, **7 (1)**, 118–128.

Ferrier, B., 1994: A double-moment multiple-phase four-class bulk ice scheme. Part I: Description. *J. Atmos. Sci.*, **51 (2)**, 249–280.

Gao, J., M. Xue, K. Brewster, and K. K. Droegemeier, 2004: A three-dimensional variational data analysis method with recursive filter for doppler radars. *J. Atmos. Oceanic Technol.*, **21 (3)**, 457–469.

Graham, R. J., S. Anderson, and M. Bader, 2000: The relative utility of current observation systems to global-scale NWP forecasts. *Quart. J. Roy. Meteor. Soc.*, **126 (568)**, 2435–2460.

Ha, S.-Y., and C. Snyder, 2013: Influence of surface observations in mesoscale data assimilation using an ensemble kalman filter. Mon. Wea. Rev., (2013), 1489—— 1508.

Hayden, C. M., and R. J. Purser, 1995: Recursive filter objective analysis of meteorological fields: applications to NESDIS operational processing. *J. Appl. Meteor.*, **34 (1)**, 3–15.

Hicks, B. Bruce, William J. Callahan, William R. Pendergrass III, Ronald J. Dobosy, and Elena Novakovskaia, 2012: Urban turbulence in space and in time. *J. Appl. Meteor. Climatol.,* **51**, 205–218, doi: 10.1175/JAMC-D-11-015.1.

Hilliker, J. L., G. Akasapu, and G. S. Young, 2010: Assessing the short-term forecast capability of nonstandardized surface observations using the national digital forecast database (NDFD). *J. Appl. Meteor. Climatol.*, **49 (7)**, 1397-1411.

Hu, M., M. Xue, and K. Brewster, 2006a: 3DVAR and cloud analysis with WSR-88D level-II data for the prediction of the Fort Worth, Texas, tornadic thunderstorms. Part I: Cloud analysis and its impact. *Mon. Wea. Rev.*, **134 (2)**, 675–698.

Hu, M., M. Xue, J. Gao, and K. Brewster, 2006b: 3DVAR and cloud analysis with WSR-88D level-II data for the prediction of the Fort Worth, Texas, tornadic thunderstorms. Part II: Impact of radial velocity analysis via 3dvar. *Mon.Wea. Rev.*, **134 (2)**, 699–721.

Iacono, M. J., J. S. Delamere, E. J. Mlawer, M. W. Shephard, S. A. Clough, and W. D.

Collins, 2008: Radiative forcing by long–lived greenhouse gases: Calculations with the AER radiative transfer models. *J. Geophys. Res.*, **113**, D13103.

Kain, J.S., and Coauthors, 2008: Some practical considerations regarding horizontal resolution in the first generation of operational convection-allowing NWP. *Wea. Forecasting*, **23**, 931-952

Kazumori, M., Q. Liu, R. Treadon, and J. C. Derber, 2008: Impact study of AMSR-E radiances in the NCEP Global Data Assimilation System. *Mon. Wea. Rev.,* **136 (2)**,541-559.

Knopfmeier, H. Ken and David J. Stensrud, 2013: Influence of mesonet observations on the accuracy of surface analyses generated by an ensemble Kalman Filter.*Wea. Forecasting,* **28**, 815-841, doi: 10.1175/WAF-D-12-00078.1.

Lang, S., & McKeogh, E. (2011). LIDAR and SODAR measurements of wind speed and direction in upland terrain for wind energy purposes. *Remote Sens.*, **3**, 1871-1901.

Lin, Y.-L., R. D. Farley, and H. D. Orville, 1983: Bulk parameterization of the snow field in a cloud model. *J. Climate Appl. Meteor.*, **22 (6)**, 1065–1092.

Lundquist, K. Julie, James M. Wilczak, Ryan Ashton, Laura Bianco, W. Alan Brewer, Aditya Choukulkar, Andrew Clifton, Mithu Debnath, Ruben Delgado, Katja Friedrich, Scott Gunter, Armita Hamidi, Giacomo Valerio Iungo, Aleya Kaushik, Branko Kosović, Patrick Langan, Adam Lass, Evan Lavin, Joseph C.-Y. Lee, Katherine L. McCaffrey, Rob K. Newsom, David C. Noone, Steven P. Oncley, Paul T. Quelet, Scott P. Sandberg, John L. Schroeder, William J. Shaw, Lynn Sparling, Clara St. Martin, Alexandra St. Pe, Edward Strobach, Ken Tay, Brian J. Vanderwende, Ann Weickmann, Daniel Wolfe, and Rochelle Worsnop, 0: Assessing state-of-the-art capabilities for probing the atmospheric boundary layer: the XPIA field campaign. *Bull. Amer. Meteor. Soc.,* **0**, doi: 10.1175/BAMS-D-15-00151.1.

Madaus, E. Luke, Gregory J. Hakim, and Clifford F. Mass, 2014: Utility of dense pressure observations for improving mesoscale analyses and forecasts. *Mon. Wea. Rev.,* **142**, 2398–2413, doi: 10.1175/MWR-D-13-00269.1.

McLaughlin, David, David Pepyne, Brenda Philips, James Kurose, Michael Zink, David Westbrook, Eric Lyons, Eric Knapp, Anthony Hopf, Alfred Defonzo, Robert Contreras, Theodore Djaferis, Edin Insanic, Stephen Frasier, V. Chandrasekar, Francesc Junyent, Nitin Bharadwaj, Yanting Wang, Yuxiang Liu, Brenda Dolan, Kelvin Droegemeier, Jerald Brotzge, Ming Xue, Kevin Kloesel, Keith Brewster, Frederick Carr, Sandra Cruz-Pol, Kurt Hondl, and Pavlos Kollias, 2009: Short-wavelength technology and the potential for distributed networks of small radar

systems. *Bull.   Amer.   Meteor.   Soc.,* **90**, 1797–1817, doi: 10.1175/2009BAMS2507.1.

Moser, Ben A., William A. Gallus Jr., and Ricardo Mantilla, 2015: An initial assessment of radar data assimilation on warm season rainfall forecasts for use in hydrologic models. *Wea. Forecasting,* **30**, 1491-1520, doi: 10.1175/WAF-D-14-00125.1.

Mukhopadhyay, P., J. Sanjay, W. Cotton, and S. Singh, 2005: Impact of surface meteorological observations on rams forecast of monsoon weather systems over the Indian region. *Meteor. Atmos. Phys.*, **90 (1-2)**, 77-108.

National Research Council, 2009: *Observing weather and climate from the ground up: A nationwide network of networks*. National Academies Press, 250 pp.

National Research Council, 2012: *Urban meteorology: forecasting, monitoring, and meeting users' needs*. The National Academies Press, 176 pp.

NOAA, 2004: National Weather Service, AWS Convergence Technologies in New Public/Private Partnership to Expand use of Weatherbug Data. Accessed 14 October   2016   [Available   online   at http://www.publicaffairs.noaa.gov/releases2004/sep04/noaa04-r299-19.html.]

NWS, 1994: Technique specification package 88-21-r2 for awips-90 rfp Appendix G requirements numbers: Quality control incoming data. AWIPS Document Number TSP-032-1992R2, NOAA, National Weather Service, Office of Systems Development.

NWS, 1999: Automated Surface Observing System (ASOS). Accessed 10 October 2016.   [Available   online   at https://www.ametsoc.org/ams/index.cfm/publications/authors/journal-and-bams-authors/journal-and-bams-authors-guide/references/.]

NWS, 2006: ACARS/AMDAR Data. Accessed 10 October 2016. [Available   online   at http://www.nco.ncep.noaa.gov/sib/restricted_data/restricted_data_sib/acars+amdar/.]

McNally, T., M. Bonavita, and J.-N. Th´epaut, 2014: The role of satellite data in the forecasting of hurricane Sandy. Mon. Wea. Rev., 142 (2), 634-646.

Mukhopadhyay, P., J. Sanjay, W. Cotton, and S. Singh, 2005: Impact of surface meteorological observations on rams forecast of monsoon weather systems over the Indian region. *Meteor. Atmos. Phys.*, **90 (1-2)**, 77–108.

Rogers, R., and M. Yau, 1989: A short course in cloud physics, international series in

natural philosophy. Butterworth Heinemann, Burlington, MA, 290 pp.

Skamarock, W. C., J. B. Klemp, J. Dudhia, D. O. Gill, D. M. Barker, M. G Duda, X.-Y. Huang, W. Wang, and J. G. Powers, 2008: A description of the advanced research WRF Version 3. *NCAR Tech. Note NCAR/TN-475+STR,* 113 pp. [doi:10.5065/D68S4MVH](doi:10.5065/D68S4MVH)

Schenkman, A. D., M. Xue, A. Shapiro, K. Brewster, and J. Gao, 2011a: The analysis and prediction of the 8–9 May 2007 Oklahoma tornadic mesoscale convective system by assimilating WSR-88D and CASA radar data using 3DVAR. *Mon. Wea. Rev.,* **139 (1)**, 224-246.

Schenkman, A. D., M. Xue, A. Shapiro, K. Brewster, and J. Gao, 2011b: Impact of CASA radar and Oklahoma Mesonet data assimilation on the analysis and prediction of tornadic mesovortices in an MCS. Mon. Wea. Rev., 139 (11), 3422—–3445.

Snook, Nathan, Ming Xue, and Youngsun Jung, 2012: Ensemble probabilistic forecasts of a tornadic mesoscale convective system from ensemble Kalman filter analyses Using WSR-88D and CASA Radar Data. *Mon. Wea. Rev.,* **140**, 2126–2146, doi: 10.1175/MWR-D-11-00117.1.

Stratman, D., K. Brewster, 2015: Impact of assimilating CASA X-Band radar data for 24 May 2011 tornadic storms using various microphysics schemes at 1-km grid Spacing. *37th Conference on Radar Meteorology*, Norman, Ok, Amer. Meteor. Soc. [Available online at https://ams.confex.com/ams/37RADAR/webprogram/Paper276178.html].

Tewari, M., F. Chen, W. Wang, J. Dudhia, M. A. LeMone, K. Mitchell, M. Ek, G. Gayno, J. Wegiel, and R. H. Cuenca, 2004: Implementation and verification of the unified NOAH land surface model in the WRF model. *20th conference on weather analysis and forecasting/16th conference on numerical weather prediction*, pp. 11–15.

Thompson, R. L., R. Edwards, J. A. Hart, K. L. Elmore, and P. Markowski, 2003: Close proximity soundings within supercell environments obtained from the Rapid Update Cycle. *Wea. Forecasting*, **18**, 1243-1261

Tyndall, D. P., and J. D. Horel, 2013: Impacts of mesonet observations on meteorological surface analyses. *Wea. Forecasting*, **28 (1)**, 254-268.

Understory, 2016: Understory Weather. Accessed 14 October 2016 [Available online at http://understoryweather.com/about/.]

Unidata, 2014: NOAA Wind Profiler Network (NPN). Accessed October 14 2016

[Available   online   at http://www.unidata.ucar.edu/blogs/news/entry/noaa_wind_profiler_network_np n.]

Weisman, Morris L., Christopher Davis, Wei Wang, Kevin W. Manning, and Joseph B. Klemp, 2008: Experiences with 0–36-h explicit convective forecasts with the WRF-ARW   model. *Wea.   Forecasting,* **23**, 407-437, doi: 10.1175/2007WAF2007005.1.

Xiao, Q., and J. Sun, 2007: Multiple-radar data assimilation and short-range quantitative precipitation forecasting of a squall line observed during IHOP 2002. *Mon. Wea. Rev*., **135 (10)**.

Xiao,Qingnong, Ying-Hwa Kuo, Juanzhen Sun, Wen-Chau Lee, Dale M. Barker, and Eunha Lim, 2007: An approach of radar reflectivity data assimilation and its assessment with the inland QPF of Typhoon Rusa (2002) at Landfall. *J. Appl. Meteor. Climatol.,* **46**, 14–22, doi: 10.1175/JAM2439.1.

Xue, M., K. K. Droegemeier, V. Wong, A. Shapiro, and K. Brewster, 1995: ARPS Version 4.0 710 User's Guide. 380 pp., URL http://www.caps.ou.edu/ARPS.

Xue, Ming, Fanyou Kong, Kevin W. Thomas, et al., "Prediction of convective storms at convection-resolving 1 km resolution over continental United States with radar data assimilation: An example case of 26 May 2008 and precipitation forecasts from spring 2009," Advances in Meteorology, vol. 2013, Article ID 259052, 9 pages, 2013. doi:10.1155/2013/259052

Xue, M., M. Hu, and A. D. Schenkman, 2013a: Numerical prediction of 8 May 2003 Oklahoma City tornadic supercell and embedded tornado using ARPS with the assimilation
of WSR-88D radar data. *Wea. Forecasting*, (2013), 39-62.

Yan, Haifan and William A. Gallus Jr., 2016: An Evaluation of QPF from the WRF, NAM, and GFS Models Using Multiple Verification Methods over a Small Domain. *Wea. Forecasting,* **31**, 1363–1379, doi: 10.1175/WAF-D-16-0020.1.

Zapotocny, T. H., W. P. Menzel, J. P. Nelson III, and J. A. Jung, 2002: An impact study of five remotely sensed and five in situ data types in the eta data assimilation system. *Wea. Forecasting*, **17 (2)**, 263-285.

Zapotocny, T. H.,W. P. Menzel, J. A. Jung, and J. P. Nelson, 2005: A four-season impact study of rawinsonde, goes, and poes data in the eta data assimilation system. Part II: Contribution of the components. *Wea. Forecasting*, **20 (2)**, 178-198.

Zapotocny, T. H., J. A. Jung, J. F. Le Marshall, and R. E. Treadon, 2007: A two-season

impact study of satellite and in situ data in the ncep global data assimilation system. *Wea. Forecasting*, **22 (4)**, 887-909.

Zhao, K., and M. Xue, 2009: Assimilation of coastal Doppler radar data with the ARPS 3DVAR and cloud analysis for the prediction of Hurricane Ike (2008). *Geophys. Res. Lett.*, **36 (12)**.

Appendix A

A.1

ARPS Input File

Table A.1: Physics parameterizations used for the 10 minute ARPS forecast in these experiments.

Microphysics	Lin et al. (1983)
Radiation	NASA atmospheric radiation longwave and shortwave
Convection	Explicitly resolved
Advection	Fourth-order in vertical and horizontal
Planetary Boundary Layer (PBL)	1.5 order TKE (Deardorff 1980)
Soil Model	2-layer diffusive soil model from Noilhan and Planton (1989)

A.2 Radiometer Data

In the experiments presented here we did attempt to assimilate data from the three available radiometers in the DFW testbed. Large differences were noted in the analyzed CAPE field when the radiometer data was assimilated compared to when it was denied in the initial experiments (Figure A.1). Specifically, there was increased instability near the radiometer sites in the experiment that did not include the radiometers. There is an apparent large difference in the temperature and dew point vertical profile from the radiometers compared to the model background field (Figure A.2). For the Midlothian radiometer profile shown here the entire profile is noticeably warmer with slightly lower lapse rates and so it appears the effect of including this data would be to decrease
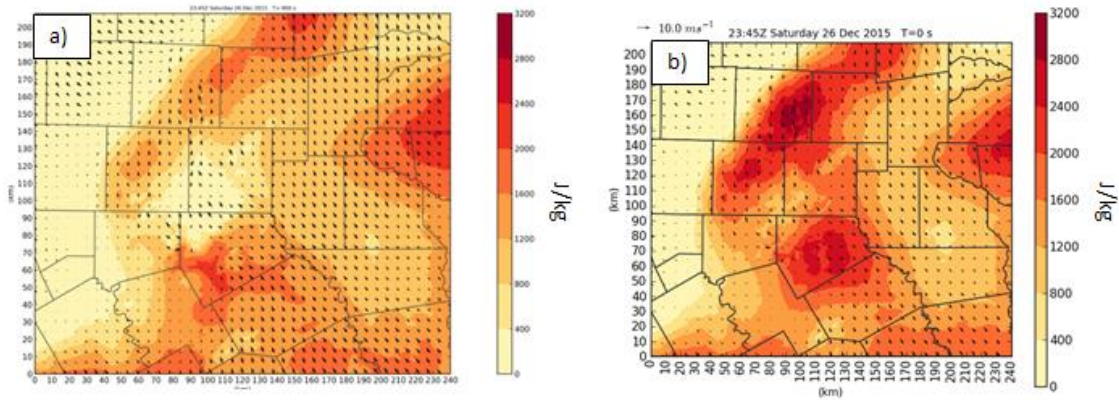
Figure A.1: Comparison of surface-based CAPE field valid at 2345 UTC for a) experiment with radiometer data and b) experiment without radiometer data.
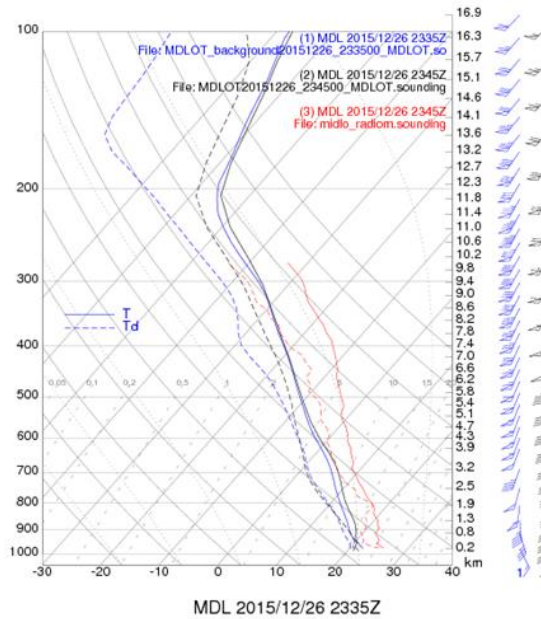

Figure A.2: Observed radiometer sounding from the Midlothian radiometer (red lines) along with the background sounding at the same location (blue lines) and the analysis sounding with radiometer data (black lines). The solid lines are temperature and the dashed lines are dew point.

instability in the overall analysis, especially in areas close enough to be strongly influenced by these observations. The instability difference translates into a difference in the forecasted 1 km AGL reflectivity field 45 minutes into the simulation (Figs. A.3). The experiments which include the radiometer data have much more of an overestimate

of reflectivity values greater than 50 dBZ compared to those without the radiometer data. This radiometer data had been assimilated for the real-time CAPS run and was likely part of the cause for the large wet bias for that forecast. Accordingly, the experiments presented here do not assimilate the radiometer data as more work needs to be done to understand how these observations should be used in the assimilation process.
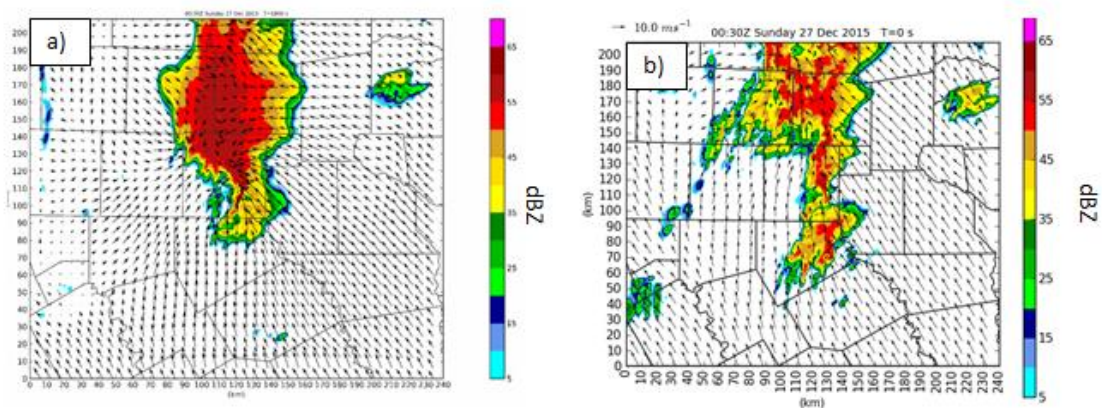

Figure A.3: Comparison of 1 km AGL reflectivity for a) experiment with radiometer data and b) experiment without radiometer data